

A Challenging Solar Eruptive Event of 18 November 2003 and the Causes of the 20 November Geomagnetic Superstorm. I. Unusual History of an Eruptive Filament

V.V. Grechnev¹ · A.M. Uralov¹ ·
V.A. Slemzin² · I.M. Chertok³ ·
B.P. Filippov³ · G.V. Rudenko¹ ·
M. Temmer⁴

Received ; accepted

© Springer ●●●●

Abstract

This is the first of four companion papers, which comprehensively analyze a complex eruptive event of 18 November 2003 in active region (AR) 10501 and the causes of the largest Solar Cycle 23 geomagnetic storm on 20 November 2003. Analysis of a complete data set, not considered before, reveals a chain of eruptions to which hard X-ray and microwave bursts responded. A filament in AR 10501 was not a passive part of a larger flux rope, as usually considered. The filament erupted and gave origin to a coronal mass ejection (CME). The chain of events was as follows: (i) a presumable eruption at 07:29 UT accompanied by a not reported M1.2 class flare probably associated with the onset of a first southeastern CME (CME1), which most likely is not responsible for the superstorm; (ii) a confined eruption (without a CME) at 07:41 UT (M3.2 flare) that destabilized the large filament; (iii) the filament acceleration around 07:56 UT; (iv) the bifurcation of the eruptive filament that transformed into a large “cloud”; (v) an M3.9 flare in AR 10501 associated to this transformation. The transformation of the filament could be due to the interaction of the eruptive filament with the magnetic field in the neighborhood of a null point, located at a height of about 100 Mm above the complex formed by ARs 10501, 10503, and their environment. The CORONAS-F/SPIRIT telescope observed the cloud in

¹ Institute of Solar-Terrestrial Physics SB RAS, Lermontov St. 126A, Irkutsk 664033, Russia email: grechnev@iszf.irk.ru
email: uralov@iszf.irk.ru

² P.N. Lebedev Physical Institute, Leninsky Pr., 53, Moscow, 119991, Russia email: slem@lebedev.ru

³ Pushkov Institute of Terrestrial Magnetism, Ionosphere and Radio Wave Propagation (IZMIRAN), Troitsk, Moscow Region, 142190 Russia email: ichertok@izmiran.ru

⁴ IGAM/Kanzelhöhe Observatory, Institute of Physics, UNI Graz email: manuela.temmer@uni-graz.at

304 Å as a large Y-shaped darkening, which moved from the bifurcation region across the solar disk to the limb. The masses and kinematics of the cloud and the filament were similar. Remnants of the filament were not clearly observed in the second southwestern CME (CME2), previously regarded as a source of the 20 November geomagnetic storm. These facts do not support a simple scenario, in which the interplanetary magnetic cloud is considered as a flux rope formed from a structure initially associated with the pre-eruption filament in AR 10501. Observations suggest a possible additional eruption above the bifurcation region close to solar disk center between 08:07 and 08:17 UT that could be the source of the 20 November superstorm.

Keywords: Active Prominences; Coronal Magnetic Fields; Filament Eruptions; Microwave and X-Ray Bursts

1. Introduction

1.1. Enigma of the 20 November 2003 Geomagnetic Superstorm

Severe geomagnetic storms are among the most dangerous space weather disturbances caused by solar activity. Impressive examples are the superstorm on 1–2 September 1859 produced by the Carrington event (Carrington, 1859), when ‘many fires were set up by arching from induced currents in telegraph wires’ (E. Loomis in Tsurutani *et al.* (2003)), and the 13–14 March 1989 superstorm, when a system-wide power blackout occurred in Quebec (Canada). Strongest geomagnetic storms develop due to the arrival of magnetic clouds (MC), which originate from solar coronal mass ejections (CMEs). In a presumable typical scenario, an MC forms from an erupting magnetic flux rope, which stretches out into interplanetary space, while its ends usually remain connected to the Sun. If an Earth-directed MC has a magnetic field component pointing South ($B_z < 0$), then magnetic reconnection between such an MC with the Earth’s magnetosphere results in a geomagnetic disturbance. The effect is considered to directly depend on the magnetic field strength and the MC velocity. Thus, eruptions involving regions of strongest magnetic fields with the favorable orientation, *i.e.*, sunspot penumbras and especially umbras, are major candidates as sources of superstorms (*cf.* Gopalswamy *et al.*, 2005c). Such events produce fast CMEs, powerful flare emissions up to gamma rays, strong radio bursts at microwaves, millimeters and even submillimeters, and energetic particles. Indeed, nine of the 11 superstorms with $Dst < -250$ nT during Solar Cycle 23 listed by Echer, Gonzalez, and Tsurutani (2008) were due to major solar eruptive events (GOES X-class flares), but those on 7 April 2000 and 20 November 2003, the latter being the strongest one during Solar Cycle 23 ($Dst = -422$ nT according to the final data of the Kyoto Dst index service, http://wdc.kugi.kyoto-u.ac.jp/dst_final/index.html), were not. These facts imply that either an amplification mechanism exists or scenarios of such events might be different from a typical one.

The 20 November 2003 superstorm was probably due to a solar eruptive event on 18 November. This event occurred during the second appearance on the

Earth-facing solar hemisphere of a decaying complex of formerly superactive regions (ARs) 10484 (10501), 10486 (10508), and 10488 (10507) (the first numbers correspond to the previous solar rotation AR numbers. We will use hereafter the last three digits of the NOAA numbers for brevity) responsible for the extreme events late in October 2003 (see, *e.g.*, Veselovsky *et al.*, 2004; Chertok and Grechnev, 2005; Gopalswamy *et al.* 2005a, 2005b; Grechnev *et al.*, 2005). Several studies (*e.g.*, Gopalswamy *et al.*, 2005c; Yurchyshyn, Hu, and Abramenko, 2005; Ivanov, Romashets, and Kharshiladze, 2006; Yermolaev *et al.*, 2005; Möstl *et al.*, 2008; Srivastava *et al.*, 2009) revealed various features of the 18 November event but have not led to a certain conclusion about the causes of its extreme geomagnetic effect. The overall scenario of the event remains unclear. The major question is why this moderate eruptive event produced an MC with a very strong magnetic field near Earth of $|B| \approx 56$ nT, extremely large southern component $B_z \approx -46$ nT, and eventually caused the superstorm. The success of a recent attempt by Kumar, Manoharan, and Uddin (2011) seems to be questionable because the conjecture about two merged MCs is not supported quantitatively, while the corresponding large outline in their Figure 16 disagrees with three reconstructions of the MC (Yurchyshyn, Hu, and Abramenko, 2005; Möstl *et al.*, 2008; Lui, 2011) as all show a compact cross section. This mysterious event urges one either to find a key to its extremity or to confess that a possible superstorm can commence unexpectedly. The only way we see in pursuing the former option is to analyze the 18–20 November complex event including eruptions, CMEs, and the interplanetary disturbance in still more detail. The event has turned out to be the most complex one among all those we ever dealt with. Its complexity and unusual properties were misleading for some previous studies. Their conclusions are compared with the observational facts presented here. We untangle the complex scenario of the whole event by following its manifestations and exclude one by one phenomena whose association with the superstorm is unlikely, as well as the corresponding conjectures considered previously. On the other hand, our results obtained in this way shed additional light on scenarios of eruptions, their course, relations between eruptions and flares, excitation of shock waves, and other important issues.

We present our study in four companion papers. The present paper (hereafter paper I) analyzes eruptions from region 501 on 18 November 2003 and their subsequent evolution. Paper II (Grechnev *et al.*, 2013, in preparation) addresses CMEs, coronal shock waves, and drifting radio bursts, which this event produced. Paper III (Uralov *et al.*, 2013, in preparation) addresses the interaction between the erupting filament and the magnetic field in the neighborhood of a coronal null point and the helicity mismatch between the MC and the pre-eruption region. Proceeding from the results of paper I–III, paper IV (Grechnev *et al.*, 2013, in preparation) tries to understand the possible causes of the extremity of the 20 November geomagnetic storm.

1.2. Challenges of Solar Eruptions

Solar eruptions are closely associated with flares and CMEs. Understanding these phenomena is important for both the fundamental science and space weather

forecasting. Despite many years of studying eruptive phenomena neither persuasive scenarios of eruptions and CME initiation nor their quantitative characteristics have been established. Relations between flares, CMEs, and accompanying disturbances remain under debate. Some observational challenges do not meet adequate theoretical expectations. All of these circumstances urge one to analyze eruptions and associated phenomena in detail, especially quantitatively.

Eruptive prominences/filaments and surges have been traditionally observed from Earth in the $H\alpha$ line and more recently in the He I 10830 Å line. These observations, limited by the loss of opacity, rarely allow measurements up to long distances. Space-borne observations in extreme-ultraviolet (EUV) coronal emission lines of Fe IX 171 Å and Fe X–XI 195 Å carried out by the *Extreme-ultraviolet Imaging Telescope* (EIT) aboard the *Solar and Heliospheric Observatory* (SOHO), the *Transition Region and Coronal Explorer* (TRACE), and recently by the *Extreme UltraViolet Imager* on the *Solar Terrestrial Relation Observatory* (STEREO) and the *Atmospheric Imaging Assembly* (AIA) on the *Solar Dynamics Observatory* (SDO) show filaments in absorption and sometimes in emission as they are heated. The He II 304 Å line is well suited to detect filaments due to its temperature sensitivity range (maximum at 80 000 K). Observations in this line were limited up to the recent time.

A typical eruptive filament (prominence) rises, expands, and departs from the Sun as a core of a CME. Filament material can partly drain back to the solar surface along stretched field lines, former legs of the filament. Sometimes the eruptive filament stops after the initial rise or returns back to the Sun (‘failed eruptions’). The magnetic structure of an eruptive filament mainly persists, although partial reconnections seem to occur both in the filament and between it and the magnetic field in the environment. Observations also suggest that occasionally an eruptive filament can transform into a large cloud, which falls back down to the solar surface far from the eruption region (Grechnev *et al.*, 2008; 2011a). This suggests dramatic changes in the magnetic structure of the filament. Such little-known anomalous eruptions have been rarely observed in the 304 Å line.

Most models of eruptions and CME initiation involve magnetic flux ropes with or without passive filaments embedded and many models invoke magnetic reconnection. However, the possible role of filaments themselves in eruptions from active regions is not highlighted by most models. This might be partially due to insufficient observational basis of the models because of the limitations mentioned above and difficulties to observe the initial phases of CMEs, as well.

The 18 November event manifested in a series of partial eruptions followed by the eruption of a large filament rooted in AR 501 (\sim N00 E18), a complex long-duration $H\alpha$ flare, and soft X-ray (SXR) bursts with two reported peaks at 07:52 and 08:31 (*all times hereafter are UT*). The *Large Angle and Spectroscopic Coronagraph* (LASCO; Brueckner *et al.*, 1995) on SOHO observed two CMEs starting at 08:06 and 08:49. Several papers addressed various aspects of this solar event, its preparation, and consequences. Hard X-ray (HXR) emission during the M3.9 two-ribbon flare (after 08:07) in relation to the energy release rate was studied by Miklenic *et al.* (2007), Möstl *et al.* (2008), and Miklenic, Veronig, and Vršnak (2009). Srivastava *et al.* (2009) analyzed the evolution of magnetic fields

in AR 501 and compared the magnetic energy budget with energetics of the flare and CME. Gopalswamy *et al.* (2005c), Yurchyshyn, Hu, and Abramenko (2005), Möstl *et al.* (2008), Chandra *et al.* (2010), and Kumar, Manoharan, and Uddin (2011) compared properties of the eruptive filament with those of the magnetic cloud which hit Earth.

The eruptions in this event were observed by several instruments, but not analyzed in most of the previous papers. Kumar, Manoharan, and Uddin (2011) started to study the eruptions, but their analysis was incomplete, and the discussions were mainly based on assumptions, although the observations allow one to carry out detailed measurements.

Our interest in the 18 November 2003 event is reinforced by the observation of a large inverse-Y-shaped dark feature moving after the eruption across the solar disk in the South-West direction towards the limb (Slemzin *et al.*, 2004). This phenomenon was recorded in 304 Å by the *Spectroheliographic X-ray Imaging Telescope* (SPIRIT; Zhitnik *et al.* (2002) and Slemzin *et al.* (2005)) aboard the *Complex Orbital near-Earth Observations of Activity of the Sun* (CORONAS-F) satellite (Oraevsky and Sobelman, 2002; Oraevsky *et al.*, 2003). Grechnev *et al.* (2005) concluded that the darkening was due to absorption of the solar emission by a cold plasma cloud formed from an eruptive filament and stated that the filament ‘probably failed to become a CME core’. This circumstance has not drawn the attention of researchers who studied the geoeffective outcome of the event. From the absorption observed in the He II 304 Å line, we estimate a density and mass of the absorbing cloud and compare it with the mass of the eruptive filament. We also compare their kinematics and analyze coronal magnetic fields. In this way we endeavor to understand what happened to the eruptive filament in order to find out in papers II–IV the causes of the very strong geoeffective outcome of this eruptive event.

Section 2 outlines observations of the solar event and reveals its important episodes. Section 3 addresses measurements of the kinematics. Section 4 studies magnetic fields. In Section 5 we compare the masses of the eruptive filament and the Y-like cloud observed in 304 Å. We summarize and discuss our results in Section 6. Section 7 presents the major outcome of the study.

2. Observations

2.1. Instruments and data

The event was observed in Kanzelhöhe Solar Observatory (KSO) with a tunable Lyot H α filter (full width at half-magnitude (FWHM) of 0.7 Å) mostly in the center of the 6562.8 Å H α line (line-of-sight velocities $V_{\text{LOS}} = \pm 16 \text{ km s}^{-1}$, the sunward direction is positive), in the blue wing [-0.365 Å , $V_{\text{LOS}} = -(0.6 - 33) \text{ km s}^{-1}$], and in the red wing [$+0.442 \text{ Å}$, $V_{\text{LOS}} = +(4 - 36) \text{ km s}^{-1}$]. On average, six line-center images and one pair in the wings were produced every minute from 07:30:32 to 09:20:18.

We use images observed with TRACE (Handy *et al.*, 1999) in the 171 Å and 195 Å channels, which respond to normal coronal temperatures. There was a gap

in the observations between 07:00:26 and 07:33:17. The field of view centered at $\sim [-200'', 0'']$ was 1024×1024 in the 171 Å channel and 768×768 in the 195 Å channel with a $0.5''$ pixel size.

CORONAS-F/SPIRIT observed simultaneously in the He II 304 Å band and the Fe IX–XI 175 Å coronal band (predominant temperature of 1 MK). SPIRIT produced one pair of images in both bands typically every 15 min which determines its opportunity to study eruptions (methods of data processing can be found in Bogachev *et al.* (2009)). We also use images of SOHO/EIT (Delaboudinière *et al.*, 1995) and the *Soft X-ray Imager* (SXI; Hill *et al.*, 2005; Pizzo *et al.*, 2005) on GOES-12, produced with a polyimide filter composition. A wide SXI passband, with a maximum at ≈ 4 MK, is sensitive to temperatures of $\gtrsim 10$ MK at a level of 20%. The sensitivity also declines to 10% at ≈ 1 MK.

Magnetic fields were studied from full-disk magnetograms produced with the *Michelson Doppler Imager* (MDI; Scherrer *et al.*, 1995) on SOHO. We study the evolution of magnetic fields on the photosphere from 1-min series of MDI magnetograms produced from 07:00 to 08:00. To analyze the coronal magnetic field, we used for extrapolations three MDI magnetograms from 96-min series observed at 06:23, 07:59, and 09:36. In spite of active photospheric motions, the coronal configuration of interest did not show significant changes. The results presented here have been obtained from the MDI magnetogram at 07:59.

2.2. A Brief Description of the Event

Active region 501 (Carrington longitude $L_0 = 2$) exhibited ongoing activity. An M4.2 SXR class and 1N H α flare, associated to a CME event, on 17 November (SXR peak at 09:05) and a series of events on 18 November occurred in this region. The main 18 November event was associated with the eruption of a large U-shaped filament (F1) that extended to the South-West of AR 501 (Figure 1a). The main eruption (after 07:55) was preceded by partial eruptions of some portions of the filament. Figure 1b reveals the eruptive filament in the far blue wing of the H α line, at least, 15 min later than the onset of its eruption. The filament looks reversed and fragmented in the inset.

A LASCO/C2 image in Figure 1c shows CME1, probably associated with one of partial eruptions, and CME2 presumably ejected during the main eruption (the onset time of CME2 extrapolated to the solar disk center was between 08:05 and 08:20 (Gopalswamy *et al.*, 2005c)). CME2 had a faster, fainter outer halo (speed ≈ 1660 km s $^{-1}$) and a brighter, slower (by about 30%) inner component. An arcade and dimmings in a later EIT 195 Å image ratio (09:11 divided by an image at 07:35) suggest eruptions and possibly other strong perturbations in the corona. CORONAS-F/SPIRIT observed a Y-like darkening in 304 Å (Figure 1d) well after the eruption and appearance of CME2.

2.3. X-ray and Microwave Time Profiles

Figure 2a presents SXR GOES light curves for a six-hour interval on 18 November. A C3.8 eruptive flare occurred in AR 501 from 05:00 to 06:00 and the series of events of interest, shown in the lower panels of Figure 2, started at 07:14 with

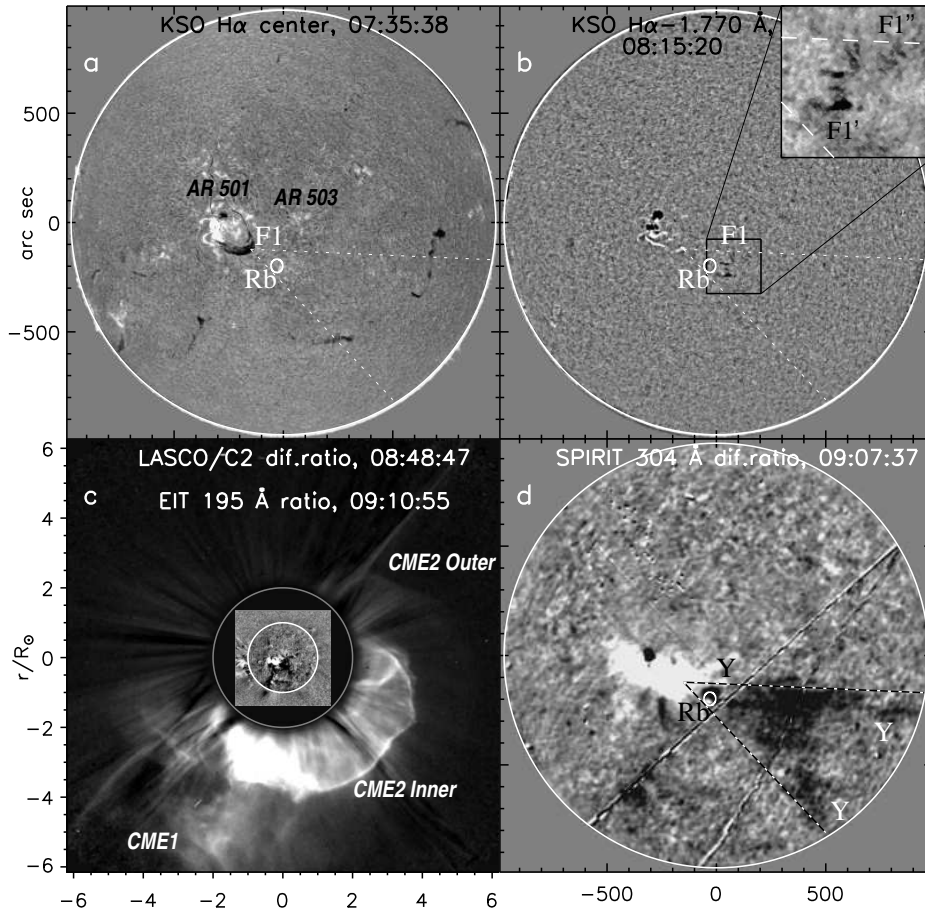


Figure 1. Overview of the event. a) The main filament F1 before eruption ($H\alpha$, KSO). A flare in the eastern part of AR 501 already started. b) The eruptive filament in the far blue wing $H\alpha$ image. Flare ribbons expanded west. c) CMEs observed with LASCO/C2 and their footprints in a later EIT 195 \AA image ratio. d) A large Y-like darkening in a CORONAS-F/SPIRIT 304 \AA image. The broken lines in panels a), b), and d) outline a sector in which the eruptive filament and the Y-like darkening were observed. The oval labeled ‘Rb’ denotes the region of bifurcation. The axes show distances from the solar disk center in arc seconds (panels a), b), and d)) and in solar radii (panel c)).

a group of type III bursts. A corresponding 2N $H\alpha$ flare was reported to occur from 07:16 to 09:55, extending from S01 E20 to N00 E18. The initial episode was weak, with an SXR class of $< C1.3$ level, and was not a conspicuous event. A later eruptive event, with an M4.5 SXR peak at 10:11, occurred at the East limb in appearing AR 508 (returning AR 486). This limb event was related to onset of a third CME, CME3 (Gopalswamy *et al.*, 2005c), which could not reach Earth.

Figure 2 shows the time profiles of the activity just described from 07:20 to 08:40 in SXR (b), HXR (c), and microwaves (d). Some of the episodes were not studied previously. GOES reported two SXR bursts of an M3.2 flare (peak

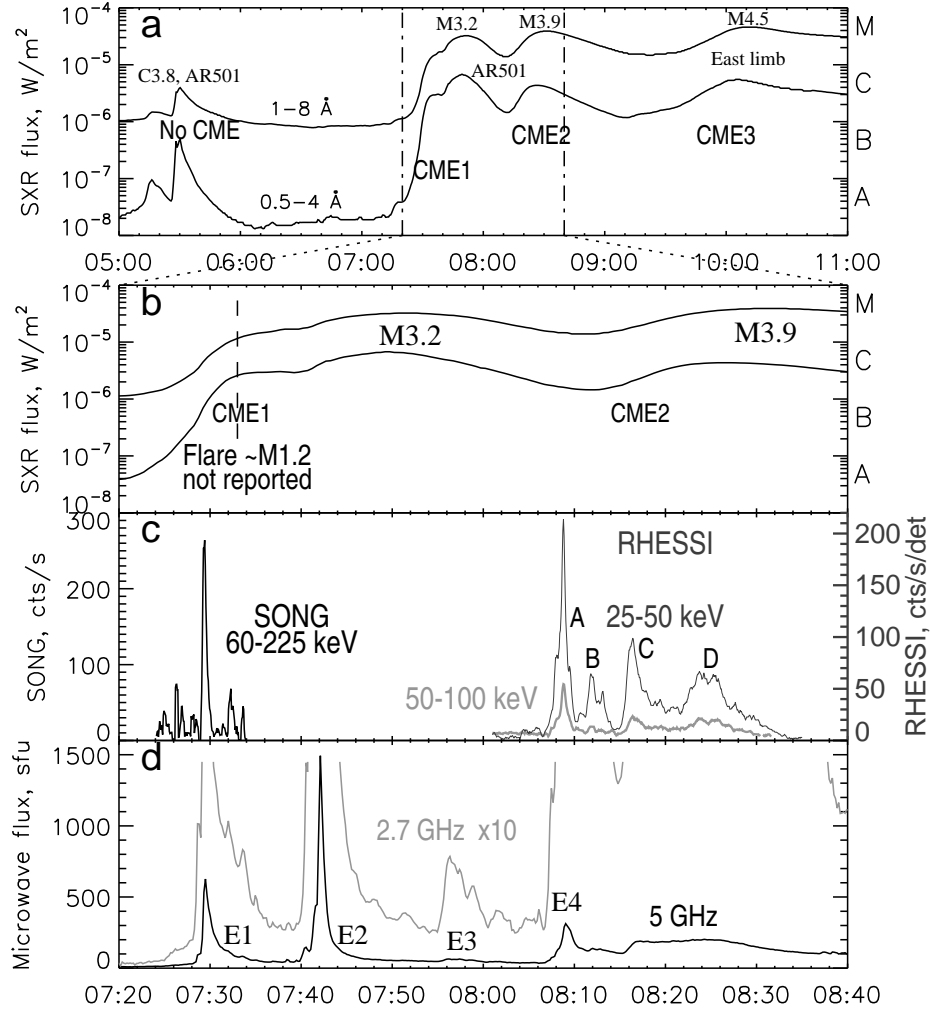


Figure 2. a) and b) GOES SXR flux, b) shows in more detail the interval between vertical dashed lines in a). c) HXR flux, the gray curve corresponds to the higher energy range. d) Microwave light curves, the gray curve in this panel shows a 2.7 GHz time profile multiplied by a factor of 10.

at 07:52) and an M3.9 flare (peak at 08:31). The *Solar Neutrons and Gamma* multi-channel detector (SONG; Kuznetsov *et al.*, 2011) aboard CORONAS-F registered a short (~ 1 min) HXR burst at 07:29. The *Reuven Ramaty High-Energy Solar Spectroscopic Imager* (RHESSI; Lin *et al.*, 2002) recorded a longer complex HXR burst starting at 08:07. No HXR data are available between 07:35 and 08:00 due to night-time intervals of both of instruments, and, therefore, we use microwaves as a proxy of hard X-rays. Microwave light curves in Figure 2d show a series of bursts recorded at 5 and 2.7 GHz in San Vito (US Air Force Radio Solar Telescope Network). The whole event consisted of four consecutive episodes, E1–E4. Their association with CMEs corresponds approximately to

the identification of Gopalswamy *et al.* (2005c) and will be confirmed in this paper and paper II.

The SXR flux of E1 reached a level of \sim M1.2. This SXR burst overlapped with the next one (M3.2 at 07:52); the SXR flux had not decreased between the two bursts and the M1.2 event was not reported. TRACE missed the corresponding eruption and we are not aware of its presence in H α observations. The presumable eruption at that time is confirmed by the appearance of the southeastern CME1. Episode E2 during RHESSI and CORONAS-F night-time was strongest in microwaves (07:42) and reached an M3.2 level. A faint episode E3 at \sim 07:57 is barely detectable in microwaves, but appears to be related to an important eruption. Episode E4 was weaker than E1 and E2, but longer (08:07–08:32), with a highest peak E4A at 08:09. The fourfold HXR burst E4 was studied in detail by Miklenic *et al.* (2007) and Möstl *et al.* (2008). The peaks of E4 are denoted A, B, C, and D according to the former paper. We show two HXR bands in Figure 2c. Higher-energy hard X-rays are known to match microwaves better; indeed, the 50–100 keV time profile is rather similar to the 5 GHz flux. Thus, microwaves can be used as a proxy of missing HXR data, but peak E4B was faint in microwaves.

To summarize, due to the intrinsically gradual character of the SXR emission (see, *e.g.*, Neupert, 1968), event E1 was not registered in soft X-rays. The SXR response to a series of HXR bursts after 08:07 merged into a single M3.9 burst. Episode E3 was too weak to be detected. Our analysis has revealed the following presumable chain of events and associations with E1–E4 (the measured eruptions started \approx 1 min before the peaks in HXR or microwaves):

- 07:29, E1. Probable eruption and CME1 onset. GOES M1.2 level.
- 07:41, E2. Confined ejection. No CME. The U-shaped filament departed. GOES M3.2 level.
- 07:56, E3. Stronger acceleration of the U-shaped filament.
- 08:09, E4A. Collision of the eruptive filament with an “obstacle” close to the solar disk center.
- 08:12, E4B. Bifurcation of the eruptive filament.
- 08:16, E4C. Presumable additional eruption above the region of bifurcation.
- 08:22–08:32, E4D. To be studied in paper II. GOES M3.9 level.
- 08:23–09:55. Moving Y-like cloud formed by filament remnants.

2.4. Partial Filament Eruptions

The U-shaped filament (or a filament system) F1 was active, except for its thin north part. An eruption in its eastern part on 17 November at about 09:00 produced an M4.2/1N flare, a jet-like ejection to the West, and a southeastwards CME with a central position angle (PA) of about 135°. Its geomagnetic effect was not pronounced. The main body of the U-shaped filament remained static.

On November 18, an eruption related to the C3.8/SF flare at 05:30 occurred also in the eastern part of AR 501 (S01E20, Figures 3a–c). Ejecta, called Ej in Figure 3, moved along the loops with ends rooted to the West of region Rb. The eruption did not originate any CME conversely to what was proposed

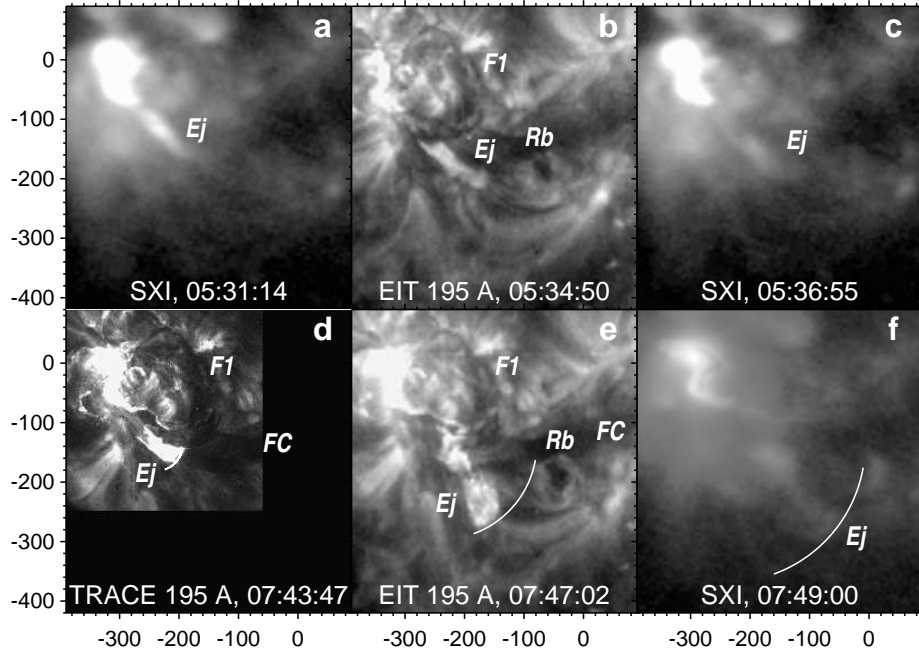


Figure 3. Homologous eruptions on 18 November: a–c) 05:30 event (C3.8 flare), d–f) 07:41 event (M3.2 flare). F1 is the main U-shaped filament, Ej are bright ejecta, Rb is the bifurcation region, FC is a static filament channel. The arc in the lower panels corresponds to the fit in Figure 11. The axes show hereafter the distances from the solar disk center in arc seconds.

by Kumar, Manoharan, and Uddin (2011), who related this flare with a slow CME which appeared at 05:26. The SOHO/LASCO CME catalog (<http://cdaw.gsfc.nasa.gov/CMElist>, Yashiro *et al.*, 2004) estimates its average speed to be 267 km s^{-1} and linearly extrapolates the onset time to 04:13 at $1R_{\odot}$ and to 03:29 at the disk center (close to AR 501). According to Zhang *et al.* (2001) and Temmer *et al.* (2008, 2010), the largest acceleration of a CME is temporally close to a related flare. The large time difference between the C3.8 flare and the onset time of this CME rules out their association.

The ejection associated with E2 at 07:41 (Figures 3d–f) was similar to the preceding eruptions. A bright ejecta moved initially to the South-West, then turned south, and after that turned west again following the way of the eruption at 05:30 traced by coronal loops.

The unreported episode E1 at 07:29 occurred also in the eastern part of AR501. Several facts suggest a related eruption. The images in Figures 4a,b indicate the development of an $H\alpha$ flare (the image produced at Aryabhata Research Institute of Observational Sciences (ARIES) is from the paper by Kumar, Manoharan, and Uddin, 2011). The color lines trace the flare ribbons and preceding structures. A small flare arcade appeared in 171 \AA between 06:57 and 07:34 (Figures 4c,d). The EIT 195 \AA image ratio in Figure 4e reveals the large-scale character of the eruption. Dimming D1 was probably due to the displacement of some long loops and eruption of some others. A complex dimming D2 extending far south suggests the eruption of large structures. According to

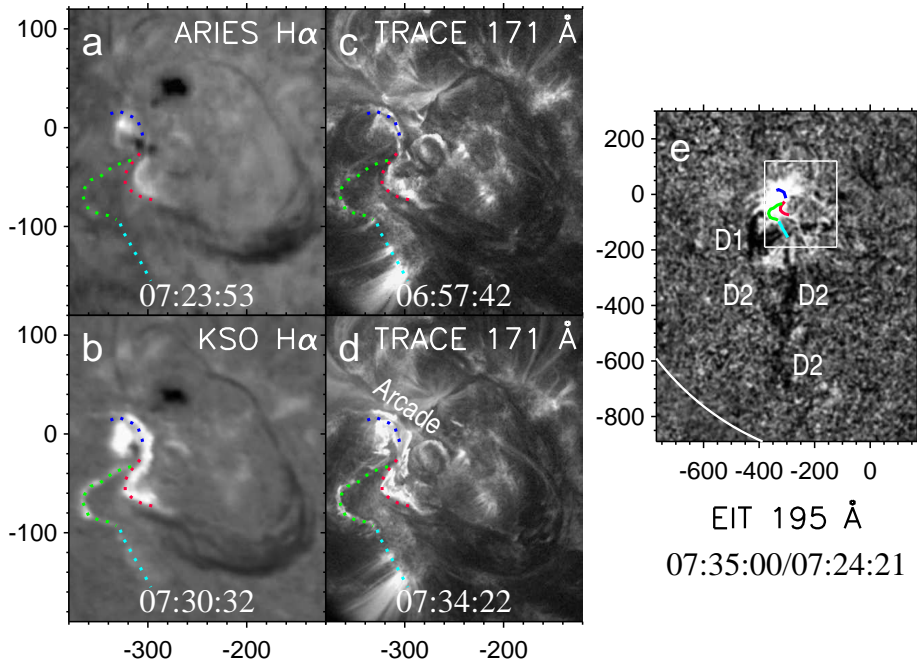


Figure 4. The not reported M1.2 eruptive event at about 07:29. a, b) Development of the flare in ARIES and KSO $H\alpha$ images. c, d) TRACE 171 Å images before and after the eruption, respectively, a post-eruption arcade is visible in c). e) Flare and dimmings (D1 and D2) in a post-eruption EIT image ratio. The color lines outline the flare brightenings and preceding structures. The frame in panel (e) shows the field of view in panels a–d.

Gopalswamy *et al.* (2005c), the onset time of CME1 at PA $\approx 168^\circ$ extrapolated to the solar disk center was about 07:22, closer to the 07:29 event than to the 07:41 eruption. Our measurements in paper II confirm this timing.

In summary, the homologous partial jet-like eruptions either had not produced any CME at all (18 November, 05:30 and 07:41) or were not geoeffective (17 November). A geomagnetic effect of the poorly observed eruption at 07:29, presumably responsible for CME1 onset, is doubtful, as discussed in paper II. The main part of the filament survived after all of these eruptions and fully erupted only after 07:55. These circumstances imply that the geomagnetic storm was most likely related to the eruption of the main filament rather than any of the preceding partial eruptions. Nevertheless, the eruption at 07:41 deserves attention, because it could destabilize the main part of the U-shaped filament and produce some observed disturbances.

2.4.1. Eruption of a Bright Jet at 07:41 (E2)

The EUV and $H\alpha$ images in Figure 5 show the eruptions after 07:30 (see also the movies TRACE.mpg, SPIRIT304.mpg, and SXI.mpg in the electronic version of the paper). The main filament initially looked similar in EUV, $H\alpha$ line center, and both $H\alpha$ wings, probably, due to the presence of internal plasma flows.

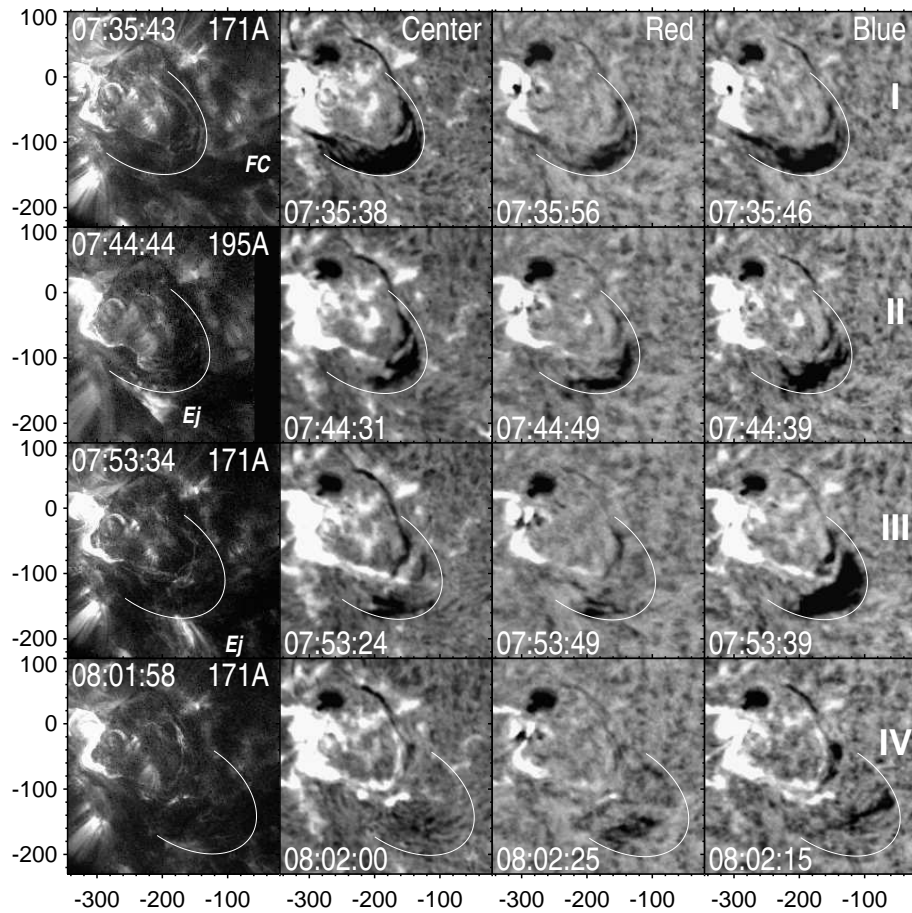


Figure 5. Eruptions E2 and E3 in TRACE and H α images. The white arc outlines the darkest part of the filament according to the solid fit in Figure 12. The shape and size of the arc correspond to the initial filament. FC is a static filament channel. Ej is a bright ejection visible in the TRACE images.

A bright jet-like feature, Ej, appeared after 07:41 in the South-East leg of the filament and moved initially along it (left column, second and third rows). Then it transformed into a bright untwisting bundle of threads and turned South. Its subsequent motion is visible in the EIT and GOES/SXI images in Figures 3e, f.

When the ejecta appeared, the corresponding portion of the filament vanished. After that the remaining part of the filament was observed to be irregular and different in H α line center and both wings. However, the filament persisted to be steady in TRACE images and only started to move slowly to the South-West. These facts suggest a perturbation of plasma flows in the filament as well as heating effects, both induced by the jet-like eruption.

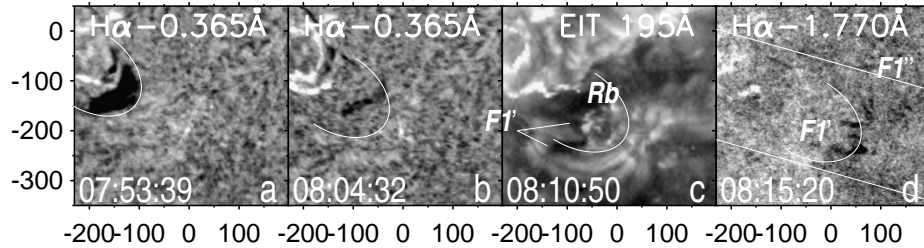


Figure 6. Motion of the eruptive filament in the blue wing of $H\alpha$ and EUV images. Rb is the region of bifurcation. Two segments starting from F1' label delimit the portion of filament F1 visible in the EIT 195 Å image c). A wide dark inclined band in this image is a static structure. F1' and F1'' are two parts of the filament (see Figure 7). The white arcs correspond to the fit in Figure 12. The white lines delimit the band used for the measurements presented in Figure 13.

2.4.2. Eruption of the Main Filament at 07:56 (E3)

Filament F1 underwent major acceleration around 07:56 and moved to the South–West losing opacity. Figure 6 shows its motion in the blue $H\alpha$ wing and an EIT 195 Å image. Our description is related henceforth to projected manifestations of phenomena which occurred at heights ~ 100 Mm. The projected trajectory of the filament crossed region Rb. Having approached this region, the eruptive filament became concave-outward in Figure 6c and then bifurcated into two parts F1' and F1'', which moved around region Rb as if this region hampered the motion of the filament's middle part. After the “collision” with region Rb, the eruptive filament looks fragmented, reverted, shifting North in the later far-blue-wing image in Figure 6d, while F1'' moved faster than F1'.

The southern filament part F1' is only visible in Figure 6c against bright coronal loops, while part F1'' is indistinguishable against a dark filament channel underneath. This static channel was separated by a wide unipolar gap from the photospheric inversion line related to the pre-eruptive filament F1. This filament channel was passive during the event. This fact is significant to identify a source structure for the 20 November magnetic cloud (paper III).

Figure 7 presents the response in the $H\alpha$ line to the collision, which occurred high in the corona above region Rb. Brightenings appeared in the southern part of this oval at about 08:07, when the approaching filament apparently contacted region Rb, and then moved clockwise by about 08:17 with a total rotation angle of $\sim 180^\circ$. The motion in region Rb is visible in both, the $H\alpha$ line center and the blue wing, but is not pronounced in the red wing; this indicates prevailing upward plasma motions. GOES/SXI images in Figure 8 also show the rotating brightenings. The coronal brightenings were more diffuse than the $H\alpha$ ones, but both coincided spatially, as the contours of the $H\alpha$ brightenings on top of the SXI images show. The SXI images show the northern filament part F1'' to roll around the bifurcation region Rb (*cf.* Figures 7c, e, f and Figures 8d, e, f). The dominant plasma temperatures in the coronal brightenings probably exceeded 1 MK, as suggested by the SXI temperature sensitivity range. Presumably, low coronal layers responded to the interaction between magnetic structures of the

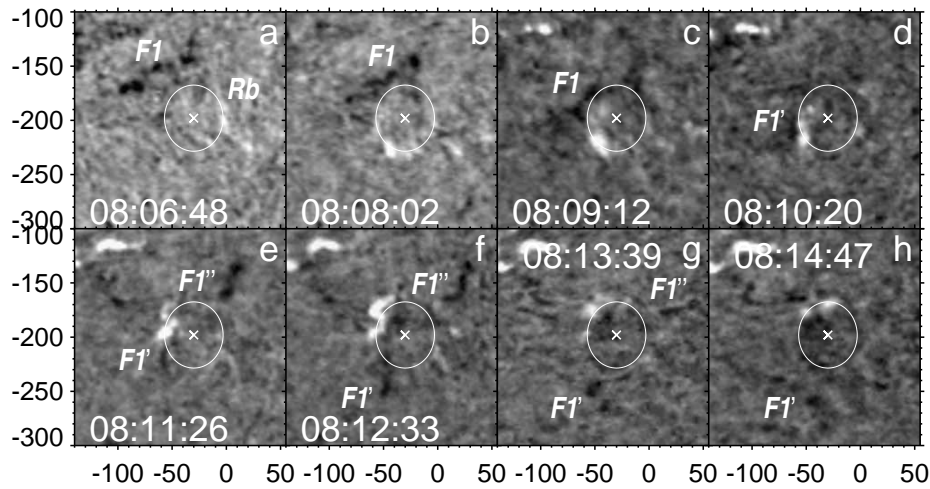


Figure 7. Bifurcation of the filament and a rotating motion underneath in the blue-wing $H\alpha$ images. F1 is the eruptive filament, F1' and F1'' are its parts after the collision with region of bifurcation Rb indicated with an oval. The slanted crosses mark the center of Rb.

filament, which moved high above the photosphere, with static coronal structures rooted in region Rb. The filament is not apparent in $H\alpha$ images after 08:16.

The rotating features were brightest at about 08:09 and 08:12, when the HXR peaks E4A and E4B occurred. Figure 8g shows $H\alpha$ light curves computed for a variable part of region Rb contoured in Figure 8h (the variance analysis was described by Grechnev (2003)) along with the HXR burst (gray). The thin black curve is the $H\alpha$ line-center time profile computed for the region within the thin contour in Figure 8h. The enhancements in the $H\alpha$ time profile correspond to the HXR peaks E4A and E4B. The correspondence is still more pronounced in the thick black time profile computed for the region within the thick contour in Figure 8h from blue-wing images observed with a lower rate. A later HXR peak E4C (light gray) had no counterpart in the bifurcation region suggesting its disconnection from AR 501 between E4B and E4C.

A difference SXI image in Figure 8i shows a dimming region which developed around region Rb from 08:11 to 08:17. This fact and the disappearance of the brightenings by 08:15 corresponding to the absence of peak E4C in the $H\alpha$ light curve in Figure 8g, suggests a possible additional eruption above the bifurcation region.

2.5. Disturbances Observed in 175 and 304 Å

Figure 9 shows CORONAS-F/SPIRIT observations. The upper row presents 175 Å image ratios. A brightening around the cross to the South-West of AR 501 in Figure 9a corresponds to the position of the eruptive filament at that time. The brightening could be due to displacement and compression of coronal loops by the expanding filament. The 175 Å images show the development of a complex dimming. The central dimming region around the cross corresponds to the

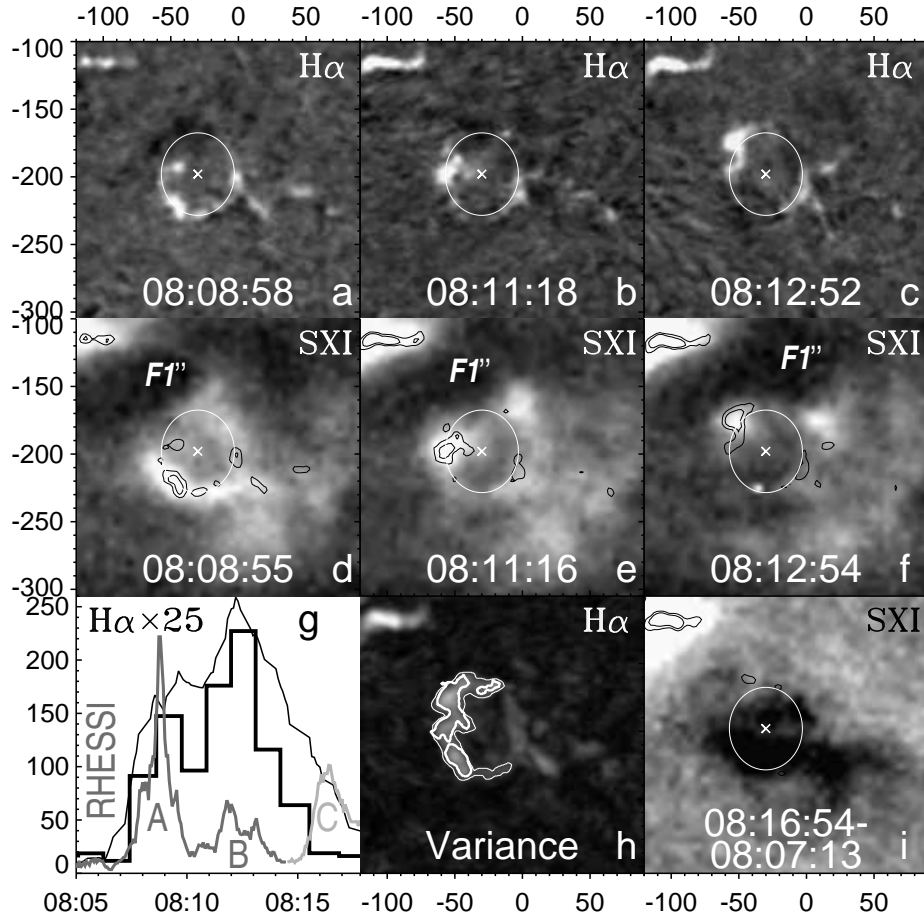


Figure 8. Flare-like phenomena in the bifurcation region in $H\alpha$ (a–c) and GOES/SXI (d–f) images. The contours on top of the SXI images outline the $H\alpha$ brightenings (levels of $1/8$ and $1/4$ of the maximum brightness). g) Time profiles in the $H\alpha$ line center (black thin solid line) and the blue wing (thick histogram) computed for the regions contoured in panel (h) with the corresponding thicknesses. The gray curve shows the RHESSI time profile in 25–50 keV. All the time profiles are quantified in instrumental units. h) Variance map computed from the line-center $H\alpha$ images. i) Dimming in an SXI difference image.

dimming in a GOES/SXI image (Figure 8i), supporting the occurrence of an eruption at that place.

The 304 \AA difference images in the lower row reveal a large dark inverted-Y-like feature moving to the South-West. It is conspicuous in Figure 9e (09:07) but appeared possibly earlier; the arc in Figure 9d hinting at its expected position at 08:23 allows one to detect a faint indication of a Y-shaped feature. The directions of motion of the eruptive filament and the Y-like feature were close to each other. No counterparts of the Y-darkening are visible in the 175 \AA images.

The changes in the shape of the Y-like feature in Figures 9d–f resemble a shrinkage because of projection in a motion along a nearly spherical surface

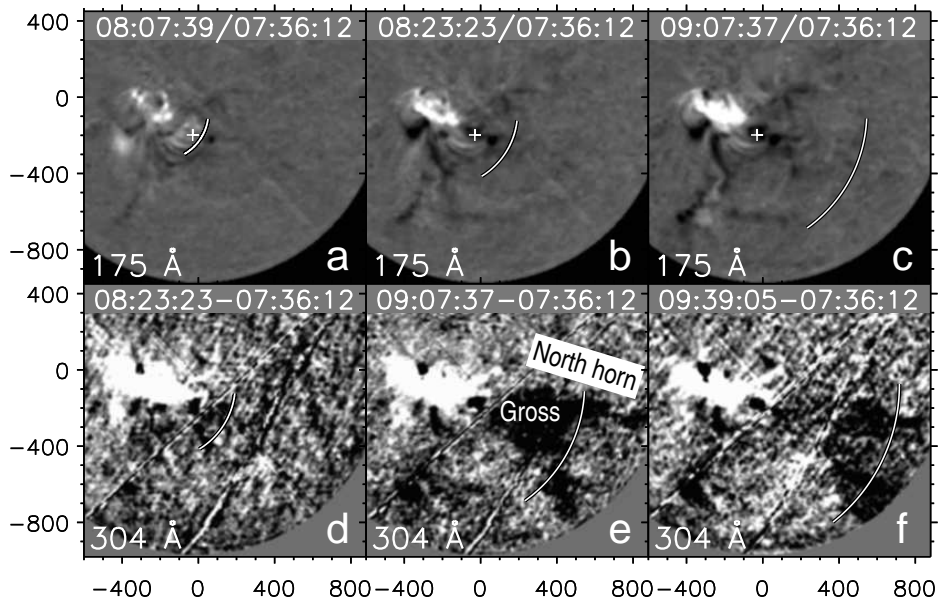


Figure 9. CORONAS-F/SPIRIT observations. The upper row shows 175 Å image ratios for the times indicated at the top of each panel. The white cross denotes the center of the bifurcation region, Rb. The lower row presents a moving Y-like darkening in enhanced-contrast 304 Å difference images. The arcs correspond to the fit shown in Figure 12. Slanted fracture-like features are due to instrumental effects.

constituted by very long closed magnetic field lines. These circumstances hint at a probable association of the Y-like darkening with the eruptive filament and its failure to leave the Sun. To verify this suggestion, we will compare the kinematics of the filament and the Y-darkening, as well as their estimated masses.

3. Kinematics

3.1. Method

Several studies (*e.g.*, Zhang *et al.*, 2001; Maričić *et al.*, 2007; Temmer *et al.*, 2008, 2010) conclude that the acceleration of a CME agrees in time with the appearance of an associated HXR burst. However, this does not guarantee the same correspondence for eruptive filaments. Grechnev *et al.* (2011b) measured accelerations of small eruptive magnetic ropes in two events to be temporally close to HXR/microwave bursts, but not to coincide with them perfectly.

The acceleration time profile is usually inferred by differentiation of distance-time measurements. This way is critical to measurement errors, temporal sampling, and provides large uncertainties. Even sophisticated methods (*e.g.*, Maričić *et al.*, 2004; Temmer *et al.*, 2010) do not overcome these difficulties completely. Our approach based on fitting an analytic function to measurements (Grechnev *et al.*, 2011b) is based on the fact that the initial and final velocities of an eruption are nearly constant and acceleration occurs within a rather short

time interval (see, *e.g.*, Figure 1b in Rompolt, 1998). We describe the acceleration with a Gaussian time profile (see Wang, Zhang, and Shen, 2009), $a = (v_1 - v_0) \exp\{-[(t - t_0)/\tau_{\text{acc}}]^2/2\}/(\sqrt{2\pi}\tau_{\text{acc}})$. Here $\tau_{\text{acc}}\sqrt{8\ln 2}$ is the FWHM of the acceleration time profile centered at time t_0 and v_0 and v_1 are the initial and final velocities. Kinematical plots are calculated by means of integration or differentiation of the analytic fit rather than the measurements. Our ultimate criterion is to follow the motion of an analyzed feature in images as closely as possible. In cases of more complex kinematics, we use a combination of Gaussians and adjust their parameters manually. The main uncertainties of the measurements are due to lamination of a filament into a multitude of expanding faint threadlike fragments that complicates following the same moving feature.

3.2. Impulsive Eruption at 07:41 (E2)

TRACE observed the eruption in the 171 and 195 Å channels (Figure 10 and TRACE.mpg and SXI.mpg movies). The initial imaging rate was relatively low (upper histogram-like plot in Figure 11a). To reduce the time interval between the two TRACE images in Figures 10a and 10c, we use a GOES/SXI image in Figure 10b. The first TRACE image shows the pre-eruptive filament. The dark filament blocked the observation of the structures behind it. The large opacity of the dark filament material indicates its low temperature, $< 2 \times 10^4$ K. There was also a bright mirrored-S-shaped feature, B_S , whose northwestern end is labeled as 1.

Portion B_{F1} of the filament South-West from 1 brightened up in Figures 10b, c indicating a temperature $\gtrsim 1$ MK, according to the sensitivity ranges of the TRACE 195 Å channel and GOES/SXI. The average plane-of-sky speed of the brightening between Figures 10a and 10b was ≥ 550 km s $^{-1}$. Motions of B_{F1} were much slower later on. These facts suggest that the rapid brightening B_{F1} over a distance of ≈ 30 Mm was most likely ignited by an MHD disturbance.

Starting from 07:41:27 (Figure 10c), the TRACE images also show another brightening B_{F2} . Initially, it was similar to B_{F1} and, later, it became a bright ejection, E_j , which is also visible in the SXI.mpg movie. In later images, the ejected structure seemed to untwist and turn South. The similar observed structure of B_{F1} and B_{F2} and their rapid appearance, followed by slower motions, indicate that both could correspond to brightenings of portions of the filament rather than to mass motions between 1 and 2. Therefore, we will compute the velocity and acceleration of E_j starting from 2 (marked in Figure 10 by a triangle).

For the measurements we extracted a slice from each image delimited by the white lines in Figure 10 and computed spatial profiles as total of the pixel values over the width of each slice. A set of the spatial profiles is shown in Figure 11a as a gray scale image in which motions of each feature are represented by a bright line, whose instant slope is the velocity. The leftmost horizontal sections correspond to the initial static condition. The measurements refer to the foremost edge of the ejection at its earliest appearance (the triangles in Figure 10).

The onset of the acceleration phase was poorly resolved. The ejection accelerated for a short time around 07:43, from $v_0 = 0$ to $v_1 \approx 450$ km s $^{-1}$. Subsequent apparent deceleration was mainly due to the turn of the ejection towards the

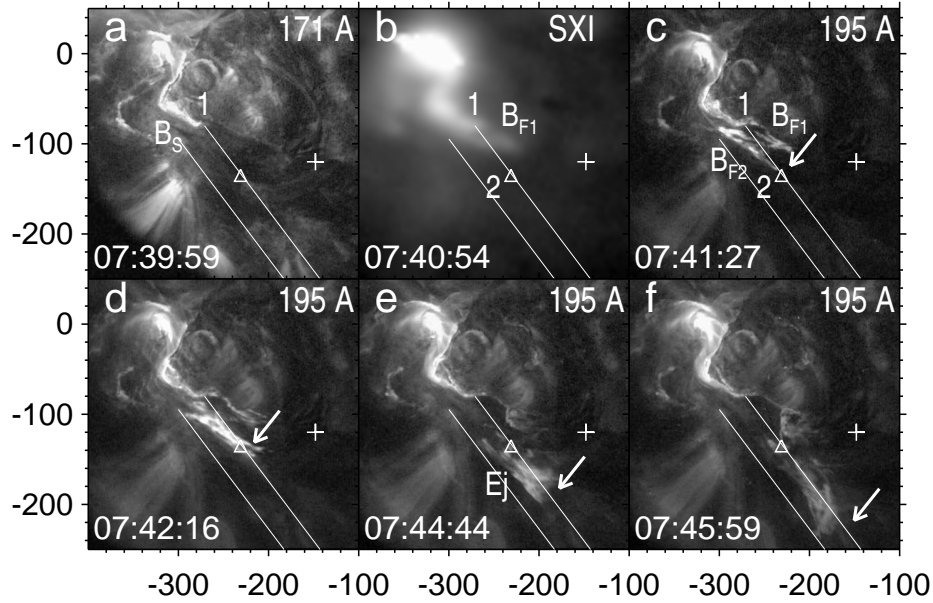


Figure 10. Impulsive eruption E2 in TRACE 171 and 195 Å and GOES/SXI images (the latter is shown in b)). The triangle is the origin of measurements. The cross marks the initial position of the filament’s top. The Solar rotation is compensated to 08:00. The arrows point to the leading edge corresponding to the fit in Figure 11. The white lines delimit a slice used in the measurements.

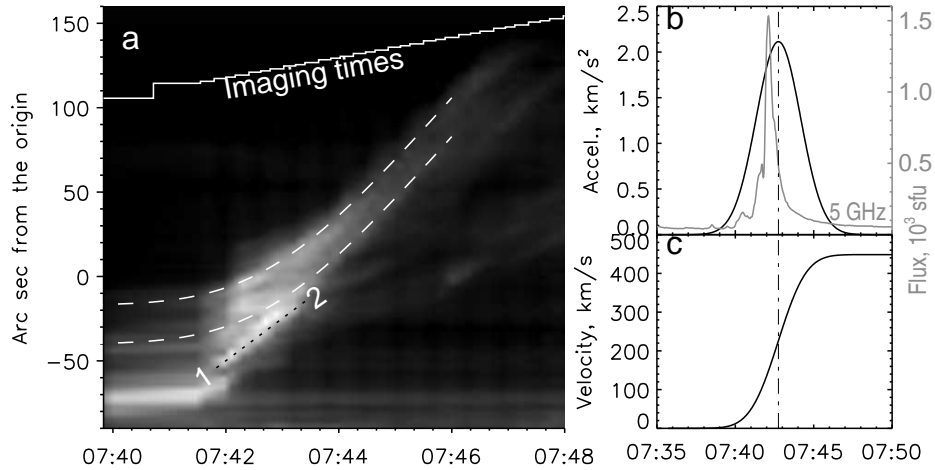


Figure 11. Plane-of-sky kinematics for ejection E2. (a) Spatial profiles computed from TRACE 171 and 195 Å images. The upper histogram-like plot shows the sampling intervals. The black dotted line 1–2 marks the feature with a sharpest apparent acceleration. (b,c) Acceleration and velocity profiles of the ejection corresponding to the white dashed curves in panel (a). The gray curve in panel (b) shows the microwave burst at 5 GHz.

South. No accelerating features, related to E2, were seen afterwards. Our fit (see Section 3.1) is shown with white dashed lines in Figure 11a and with the white arrow in Figure 10, where it acceptably matches the “nose” of the ejecta. Acceleration and velocity are plotted in Figure 11b,c. The acceleration phase was co-temporal with the microwave burst and exceeded 2 km s^{-2} ; deviations of the real shape from the assumed smooth Gaussian would imply a higher value. The apparent “jump” of the ejection (line 1–2 in Figure 11a) from the initial zero speed to $\approx 300 \text{ km s}^{-1}$ (in the plane of the sky) could really produce a shock.

The measured velocity and acceleration match those of E2 in Figure 3e and f up to its latest manifestation at 07:49, when it moved along closed loops toward their West bases. This direction was different from the orientation of CME1. The properties of E2 show its confined character. This is incompatible with the suggestion of Kumar, Manoharan, and Uddin (2011) about the role of this eruption in the formation of the 20 November magnetic cloud.

3.3. Eruption of the Main Filament at 07:56 (E3)

Comparison of the edge of the main filament in Figure 10 with the reference cross shows that its slow motion started at about 07:42, being probably triggered by eruption E2. Then, the filament accelerated around 07:56. With excellent coalignment and temporal coverage of TRACE images, measurements are hampered by the very low contrast of the filament. On the other hand, the filament appears irregularly in $\text{H}\alpha$ images, which suffer from atmospheric effects. These problems complicated the measurements.

Using the fact that the filament accelerated twice at about 07:42 and 07:56, we adjusted the parameters of the two acceleration episodes to follow the darkest filament part in both TRACE and $\text{H}\alpha$ images. We tuned the direction of the measurements from -31° to -37° relative to the West. The result is shown in Figures 5 and 6 with the white arc, whose shape corresponds to the initial filament. The kinematic plots are presented in Figure 12 with solid lines (extensions after 08:16 will be discussed later). The symbols show straightforward measurements.

When the filament started to move, its lamination became more pronounced. Some threadlike features lagged behind the gross part, while some others started to accelerate later, but outran the gross part. This picture, along with partial jet-like eruptions, does not correspond to what is expected if the filament was pulled up as a passive structure inside an expanding larger magnetic flux rope. Fit in Figure 12 presents the averaged kinematics of the eruptive filament.

We also measured the motion of the fastest filament’s part F1'' (Figures 6d and 7) detectable in the red-wing $\text{H}\alpha$ images. To catch most parts of the expanding filament, a wide band inclined by -17° to the West was used in the measurements (Figure 6d). This direction corresponds to the North horn of the Y-like darkening. A set of the measured spatial profiles is shown in Figure 13. The fastest part of the eruptive filament had a nearly constant velocity of about 210 km s^{-1} (dotted line) after the collision with region Rb. The solid line corresponds to the filament’s top measured at -37° (the maximum velocity $\approx 110 \text{ km s}^{-1}$,

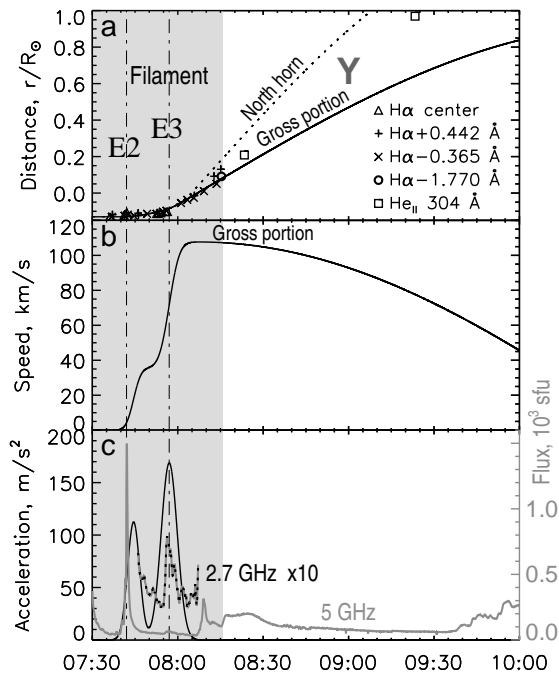


Figure 12. Apparent plane-of-sky kinematic plots of the main eruption at 07:56. E2 and E3 denote the times of the events according to Figure 2d. Apparent deceleration after 08:20 is due to projection shrinkage of the dark Y-feature moving along a curved trajectory (a circular trajectory is assumed for simplicity) and is not shown on the acceleration plot.

Figure 12b). The irregular appearance of the ragged F1'' does not allow us to plot its kinematic properties in detail, as we did for the filament's top. The maximum acceleration of $\gtrsim 500 \text{ m s}^{-2}$ occurred after 08:02, presumably when the filament touched a coronal structure above region Rb.

The kinematic analysis of filament F1 excludes its direct participation in CME2; although the filament accelerated rather close to the onset time of CME2 (Gopalswamy *et al.*, 2005c), their speeds differed by an order of magnitude. However, motion of the filament is consistent with that of the Y-like darkening inferred from the SPIRIT He II 304 Å images (squares in Figure 12a). The motion of F1'' (from Figure 13) is shown with the dotted line in this plot.

An apparent shrinkage, due to projection, of the Y-feature in Figure 9d–f suggests that its motion is nearly parallel to the photosphere. In this case, its plane-of-sky velocity is affected by the cosine of its position angle. Assuming the surface velocity to be constant, we can extend the plots in Figure 12 to the South-West up to the limb. The extrapolated fit of the filament gross portion is shown by the white arcs in Figure 9 that match the middle part of the Y-darkening. The dotted fit of the fastest filament's part in Figure 12a reaches the limb at about 09:07, this corresponds to the North horn of the Y-feature in Figure 9e.

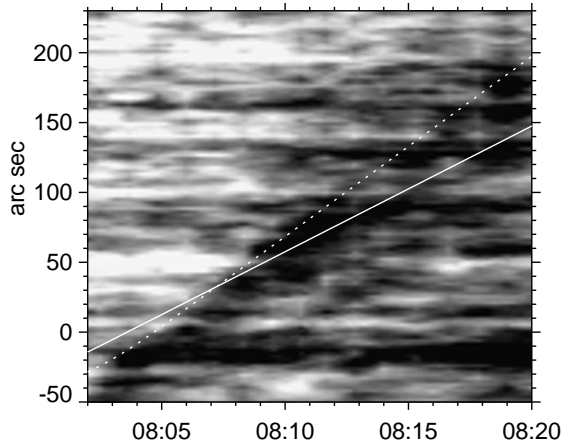


Figure 13. A set of spatial profiles of the main eruption computed from the red-wing $H\alpha$ images parallel to the North horn of the Y-like darkening (-17° relative to the western direction, the white line in Figure 6d). The dotted line fits the fastest motion. The solid line corresponds to the fit in Figure 12 related to the direction of the filament’s top (-37°).

4. Magnetic Fields

4.1. Pre-eruptive Filament

Increasing evidence confirms that filaments are directly related to coronal magnetic flux-ropes (see, *e.g.*, Mackay *et al.*, 2010). Imaging observations reveal prominences and filaments whose plasmas emit or absorb radiation thus making them most accessible indicators of magnetic flux-ropes in the corona. A loss of equilibrium of a flux-ropes shows up as a filament eruption. An eruption appearing before the onset of a flare or CME is a first manifestation of a solar storm.

The height of a filament above the photosphere is a crucial parameter to characterize its stability. Models of equilibrium of flux ropes in the corona imply the existence of a critical value of the total electric current and its relation with a critical height of a filament (van Tend and Kuperus, 1978; Molodensky and Filippov, 1987; Filippov and Den, 2001; Démoulin and Aulanier, 2010). The critical height, h_c , characterizes the size scale of the ambient coronal field.

It is not easy to measure the height of a filament observed on the solar disk. One of few possible ways is to use information about the tilt of the symmetry plane of a filament with respect to the vertical by means of the technique proposed by d’Azambuja and d’Azambuja (1948), and then to estimate the height of the filament from its observed width at any time. Zagnetko, Filippov, and Den (2005) found that the symmetry plane of a filament nearly coincided with the neutral surface of the coronal potential magnetic field or the surface that passes through the apex of magnetic field arches. Therefore, a potential extrapolation can be used to find the tilt and height of a filament.

We have used the MDI magnetogram at 07:59 as boundary condition for a potential field extrapolation (Filippov and Den, 2001). The KSO $H\alpha$ filtergram observed at 07:39:51 was carefully coaligned with the magnetogram using

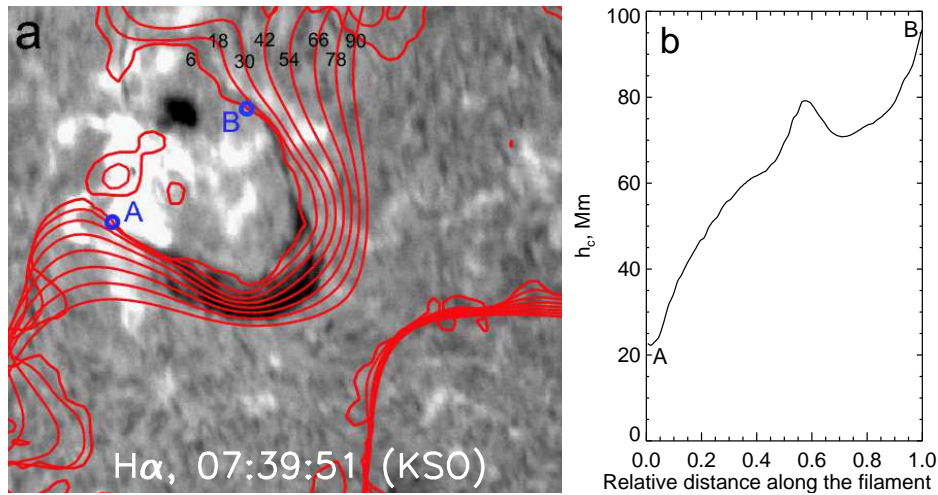


Figure 14. (a) Polarity inversion lines at different heights above the photosphere in steps of 12 Mm starting from 6 Mm (extrapolated from the MDI magnetogram observed at 07:59) overlaid on top of the KSO H α filtergram (07:39:51). (b) Values of the critical height h_c along the filament from point A to point B in panel (a). The horizontal axis shows a dimensionless relative distance measured from point A (0) to B (1).

sunspots and bringing bright flocculus kernels into coincidence with magnetic elements of the network. Figure 14a shows the H α image overlaid with a set of polarity inversion lines calculated for different heights above the photosphere starting from 6 Mm in steps of 12 Mm. The inner edge of the filament nearly coincides with the 6 Mm inversion line, while its outer edge corresponds to a height of 78 Mm. The set of lines in Figure 14a constitutes a neutral surface of the magnetic field. It is inclined in the middle part by $\approx 60^\circ$ to the photosphere. Figure 17 presents the neutral surface in more detail.

Figure 14b shows values of the critical height calculated in the way described by Filippov and Den (2001) along the filament from point A to point B in Figure 14a. The critical height was minimum in the southern part of the filament between small sunspots of opposite polarities, close to point A. The gradient of the magnetic field was high there and this site was the best place for initiation of an eruption. Even though the height of the filament was low (below the instability threshold, Figure 14), the eruption started in this part. In the North segment, the critical height was maximum; while the filament was low. This segment was very stable and did not erupt. The middle part of the filament had both largest width and height. It was close to the limit of stability. A small disturbance could be sufficient to drive an eruption.

4.2. Variations of Magnetic Fields on the Photosphere

Srivastava *et al.* (2009) and Chandra *et al.* (2010) reported significant variations of the magnetic fields in AR 501 during a few days preceding the event. To complete this picture, we analyzed a set of 60 1-min line-of-sight SOHO/MDI magnetograms between 07:00 to 08:00, using a variance technique (Grechnev

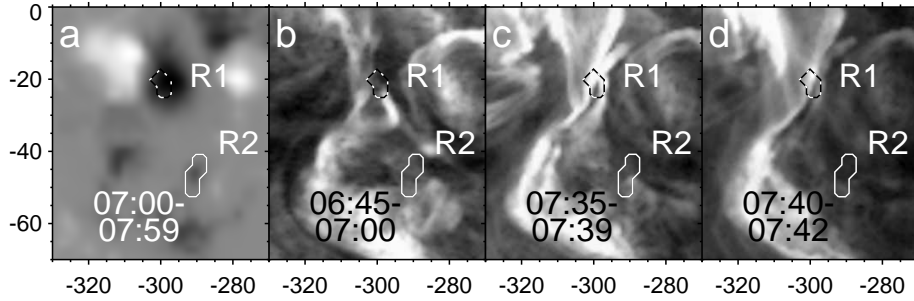


Figure 15. Contours of regions R1 and R2 (3σ level) overlaid on a magnetogram averaged along 1 hour (a) and averaged TRACE images in 171 \AA obtained before episode E1 (b), after E1 (c), and in 195 \AA averaged during episode E2 (d).

(2003); MDI magnetograms were analyzed with this technique by Kundu *et al.* (2001) and Meshalkina *et al.* (2009)). The solar rotation was compensated in all the magnetograms, and then the standard deviation was computed along each pixel in the data cube. Regions exceeding the 3σ level in the resulting two-dimensional map present most variable areas in the magnetograms. The largest changes in the line-of-sight component (B_{\parallel}) correspond to regions R1 and R2 near the filament (Figure 15). Indeed, the TRACE images in Figures 15b,c show drastic changes in the corona above R1 during episode E1. Variations in R2 might have affected a filament barb, but changes near R2 in the TRACE images in Figures 15b–d are inconclusive. Quantitative parameters of R1 and R2 are presented in Figure 16.

The B_{\parallel} component in region R1 changed significantly around 07:27 and 07:38, just before episodes E1 and E2. Region R2 was a magnetic element moving South by $\approx 2''$ from 07:00 to 08:00. A deviation of its motion occurred at about 07:41, at the onset of the eruptive event E2. The B_{\parallel} component in region R2 gradually increased, probably indicating variations of the slope of magnetic field lines. Regions R1 and R2 were close to point A in Figure 14a, *i.e.*, the South-East end of the filament. As shown in Section 4.1, this part of the filament was nearly unstable. Thus, the photospheric motions could trigger eruptions E1 and E2. In turn, disturbances produced by eruption E2 could drive eruption E3 of the major central part of the filament that was close to the limit of stability.

4.3. Neutral Surface

Threads of filaments are known to be located along inversion lines, *i.e.*, loci of null radial magnetic component, $B_r = 0$. By combining a set of magnetic neutral lines calculated at different heights, one gets a neutral surface. The shape of the neutral surface is determined by large-scale connections in a magnetic complex consisting of ARs 501, 503, and their environment (Figure 1a). The neutral surface computed in the potential approximation (Rudenko, 2001) from the MDI magnetogram observed at 07:59 is shown in Figure 17. The neutral lines at eight height levels are shown with different colors and line styles. The surface had a saddle shape resembling a hyperbolic paraboloid. The `nl_movie1.gif`

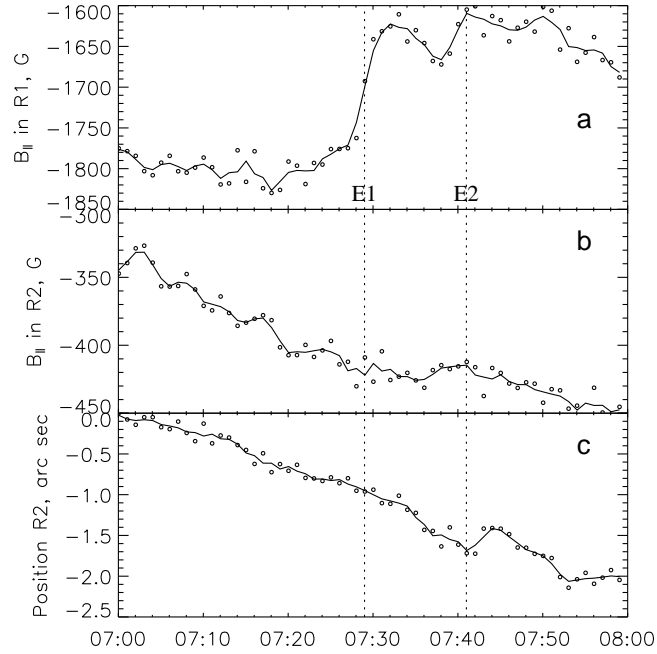


Figure 16. Variations of the line-of-sight magnetic component B_{\parallel} in regions R1 (a) and R2 (b, see Figure 15) and the displacement of the magnetic element R2 (c).

movie facilitates understanding the complex arrangement of the neutral lines at different heights in the corona (heliocentric distances are shown in the lower right corner). A topological discontinuity in B_r occurred at $1.2015R_{\odot}$. The projected location of the saddle structure was close to the bifurcation region Rb.

Having a moderate velocity, an eruptive filament lifts off presumably along a neutral surface (Filippov, Gopalswamy, and Lozhechkin, 2001, 2002; Filippov and Koutchmy, 2002). This ensures its integrity and determines the trajectory, which is sometimes erratic. When an eruption acquires significant kinetic energy, its motion becomes independent of coronal structures. The shape of the neutral surface was a topological obstacle for the moving filament. It had to undergo dramatic changes after passing through the saddle part of the configuration shown in Figure 17. A significant part of the magnetic field in the filament could reconnect with external magnetic fields. This process could result in magnetic field lines passing inside the eruptive filament and ending far on the solar surface. Part of the filament plasma moved along these field lines.

The saddle shape of the neutral surface indicates the presence of a topological singularity in the large-scale magnetic configuration. Here the singularity is a null point initially located at a height of ~ 100 Mm, as discussed in paper III. Region Rb was close to the point where the spine field line leaving the null point entered the photosphere. The projected positions of the null point, the discontinuity of the B_r component, and region Rb were close to each other.

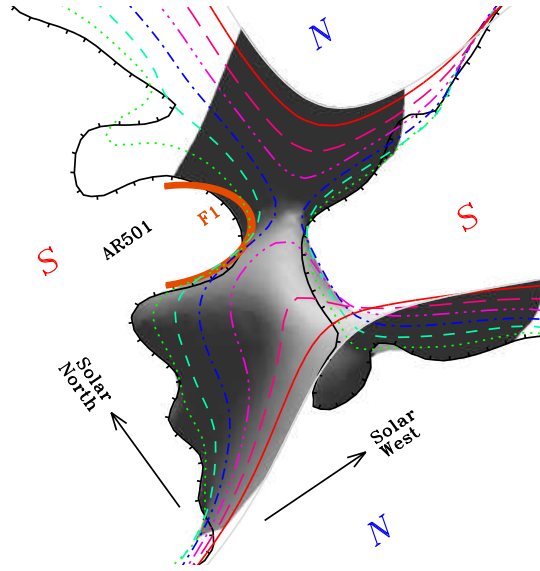


Figure 17. Magnetic neutral surface in the corona computed in the potential approximation. The orange thick arc denotes the pre-eruptive filament F1. The projection corresponds to a synoptic magnetogram rotated by 75° around the X axis (East–West) and by 35° around the Z axis (perpendicular to the photospheric X–Y plane). Neutral lines of the same color and style correspond to equal heights in steps of 36 Mm. The blue ‘N’ (positive) and red ‘S’ (negative) denote predominant magnetic polarities on the photosphere. Minor magnetic islands are not shown. The photospheric basis of the shaded neutral surface is from $L = -18.7^\circ$ to 29.1° (Carrington longitude) and from $\varphi = -40.9^\circ$ to 8.2° (latitude), *i.e.*, $\approx 580 \times 600 \text{ Mm}^2$.

5. Absorption in $H\alpha$ and EUV and Mass Estimations

The fact that the filament was dark in the $H\alpha$ line indicates a temperature $< 2 \times 10^4 \text{ K}$. Emission from such a filament is a sum of the chromospheric radiation, partly attenuated by the filament, and its own emission due to collisional or radiative excitation of hydrogen atoms. A stationary filament is usually modeled as a vertical plane-parallel slab with its height being larger than its width. When a filament activates and loses its shape, it is reasonable to consider it as a cloud. Several authors (Mein *et al.*, 1996; Molowny-Horas *et al.*, 1999; Heinzel, Anzer, and Schmieder, 2003a, and others) developed non-LTE models to relate the brightness in the $H\alpha$ line of such a cloud against the background solar disk to its parameters such as the density of neutral atoms, temperature, pressure, and velocities of turbulent and macroscopic motions.

5.1. Mass of the Pre-eruptive Filament

The pre-eruptive filament in Figure 5 (row I) had a projected distance between ends of about 100 Mm and a width of up to 37 Mm. We estimated the filament mass (without its static North-West part) at this stage from its opacity by using an approximate method based on large grids of non-LTE magneto-hydrostatic models of cool filament-like structures (Heinzel *et al.*, 2003b). The average brightness ratio of the filament to its surroundings at 07:30 was 0.85 ± 0.05 . To find

the optical thickness in the $H\alpha$ line center, we firstly calculated the parametric dependence of the total absorption in the $H\alpha$ line within the filter bandwidth on the optical thickness in the line center. The parameters were the bulk velocity of the filament, V , its turbulent velocity, V_{turb} , and temperature T . Based on these data and assuming $T \approx 6000 - 10000$ K, $V = 0$, $V_{\text{turb}} < 10$ km s $^{-1}$, and taking into account the filter bandwidth, we have estimated the optical thickness of the filament in the $H\alpha$ line center to be $\tau_0 = 0.45 \pm 0.1$.

The dimensions of the filament and its thickness along the line of sight are necessary for further considerations. The heights of the filament edges were estimated by comparing the visible filament with the height distribution of the magnetic neutral lines (see Figure 14a). Assuming the edges of the filament to coincide with the neutral lines at the same height, we found a height of 6 Mm for the lower edge, 66–76 Mm for the upper edge, and adopted an average height of 70 Mm. The brightness distribution across the broadest part of the filament can be reproduced if the filament is considered as a slab with a width of 12 Mm, height of 66 Mm, and an angle to the line of sight of $\approx 23^\circ$. With these parameters, the average line-of-sight thickness is ≈ 30 Mm.

Another assumption concerns the filament’s temperature, which determines its ionization state and the Doppler width of the $H\alpha$ line; the latter can be increased by turbulent motions. With a temperature of the filament of $T = 8000$ K (a middle value for the model used) and zero turbulent velocity, the mass of the initial filament¹ is $M_{H\alpha} = (2 - 4) \times 10^{15}$ g. This estimate refers to the cold filament body. It is embraced by a hotter plasma shell, which is a transition region between the filament and the ambient hot corona. The shell (sometimes termed the ‘EUV filament channel’) is not visible in $H\alpha$ but is considered to contribute up to 50–100% of the mass of an erupting filament (Aulanier and Schmieder, 2002). Taking this contribution into account, we estimate the total initial mass of the static filament to be $M_{\text{fil}} = (4 - 6) \times 10^{15}$ g.

The filament was also visible as a dark absorbing feature in the TRACE 171 Å and 195 Å images (Figure 5, left column), and the opacity in EUV can be used to estimate its mass as well (Anzer and Heinzel, 2005). At the assumed temperature of 8000 K, the darkening of a filament in coronal EUV lines can be due to two factors: *i*) absorption of EUV continuum radiation from underlying coronal layers by neutral hydrogen and helium, and *ii*) the absence of the coronal emission from the volume of the filament (‘volume blocking’ effect). The latter fraction depends on the heights of the lower and upper edges of the filament estimated above. Assuming that the corona is uniform and the scale height is 40 Mm, the filament mass estimated from EUV opacity is $(1 - 2) \times 10^{15}$ g, somewhat less than the estimate from the $H\alpha$ opacity. This is probably due to bright loops located above the filament and nearby, whose presence causes overestimation of background and underestimation of the optical thickness of the filament.

¹Hereafter the error ranges correspond to uncertainties in opacity measurements. Masses estimated in terms of this approximation agree with those estimated by means of different methods within a factor of 2. The accuracy of relative variations of masses estimated from single-wavelength images is considered to be considerably higher.

5.2. Y-like Darkening at 304 Å

The filament accelerated around 07:56, and after 08:01 some of its parts appeared in the red channel. Between 08:07 and 08:10 (E4A) the filament reached region Rb (Figure 7) where it bifurcated and presumably separated into a multitude of pieces detectable in both the blue and red wings, and after 08:16 it completely disappeared from the H α line.

The Y-like darkening visible from 08:23 to 09:54 in the SPIRIT 304 Å images (Figures 9d–f) had no detectable counterparts in the H α channels. The area of the darkening at 304 Å was maximum at 09:07 (Figure 9e), when the average ratio of its brightness to the background was 0.84. The horizontal velocity of the major part of the cloud at that time was between 110 and 60 km s⁻¹ (Figure 12a,b).

Analysis of absorption mechanisms in the He II 304 Å line (Grechnev *et al.*, 2008) shows that a darkening in this line can be due to two processes: *i*) non-resonant absorption of incident continuum emission in hydrogen and helium, and *ii*) resonant scattering of the He II emission irradiated by the whole solar hemisphere on the He II ions in the cloud. The latter mechanism alone provides a depression of $2\pi/4\pi = 0.5$. With a line-of-sight velocity of the cloud > 50 km s⁻¹, the Doppler shift of the He II 304 Å line in the cloud from the emission line diminishes the resonant scattering. The absence of the cloud in any of the H α channels indicates its rather high vertical velocity. Thus, the darkening in the He II 304 Å line was mainly due to the non-resonant absorption.

The average depressed brightness within the darkening of 0.84 corresponds to the optical thickness of $\tau_{304} = 0.17$. Assuming the non-resonant absorption mechanism, with an average absorption cross section of $\sigma_{304} = 5.5 \times 10^{-19}$ cm² for the 90% H + 10% He mixture (Anzer and Heinzel, 2005), we obtain the total column number of atoms $N = 3 \times 10^{17}$ cm⁻². With a thickness of the absorbing layer of the order of 10 Mm, this corresponds to a reasonable gas density of $n = 3.6 \times 10^8$ cm⁻³. Integration over the total area of the absorbing feature gives a cloud mass of $M_{304} = (2 - 4) \times 10^{15}$ g from the 304 Å data.

Though no darkening was visible in the SPIRIT 175 Å coronal images, their processing revealed absorption with an average optical thickness of $\tau_{175} = 0.02 - 0.2$. The mass of the cloud estimated from the 175 Å data is $M_{175} = (1 - 9) \times 10^{15}$ g with a middle value of 5×10^{15} g, which agrees with the M_{304} within the accuracy of the estimation. These estimates refer to the total mass of the cloud including the surrounding EUV filament channel, because EUV radiation is absorbed with nearly the same cross section by plasmas with temperatures of up to 8×10^5 K.

In summary, the average mass of the Y-like cloud absorbing EUV emission, $(2 - 4) \times 10^{15}$ g, was close to the mass of the pre-eruptive filament visible in the H α line. Minor fractions of the initial mass could be carried away by the ejecta which erupted at 07:41 and by fastest filament fragments (possible absorbing material above the limb or behind it was not visible in the image used in the measurements). Heated material invisible in EUV can contribute to the total mass. Thus, cool material of the Y-like cloud inherited the major part of material of the main filament.

6. Summary and Discussion

Variations of the photospheric magnetic fields suggest that eruption E1 at 07:29 as well as eruption E2 at 07:41 might have been triggered by photospheric motions. The E1 event was presumably associated with a partial eruption from the easternmost region of filament F1 and the launch of CME1 in the southeastern direction. The eruption manifested in short HXR and microwave bursts and an SXR enhancement with an M1.2 level (which was not reported).

Episode E2 started with rapid brightenings of long segments in the South-South-East part of the filament visible in TRACE and SXI images (similar brightenings of eruptive filaments are often observed). The average propagation speed of the brightening was $\geq 550 \text{ km s}^{-1}$. These circumstances suggest heating in the brightened part of the filament from an initial temperature of $< 2 \times 10^4 \text{ K}$ up to $\gtrsim 1 \text{ MK}$. Heating could be caused by some process (possibly associated with magnetic reconnection) in the filament or below it rapidly ignited over a long distance by an MHD disturbance. A volumetric fraction of the heated part is unknown, skin-heating is probable (Grechnev *et al.*, 2006). Heating must result in a rapid increase of the plasma pressure, $2nkT$, by about two orders of magnitude. Thus, heating alone could cause the plasma ejection along the magnetic field.

The impulsive eruption E2 started by 07:41:27, before the peak of the related microwave burst (Figure 2d). Acceleration of the ejecta reached $\approx 2 \text{ km s}^{-2}$ at about 07:43 to reach its final speed of $\approx 450 \text{ km s}^{-1}$ in the plane of the sky. The microwave burst was also short and co-temporal with the acceleration pulse. The SXR emission reached the M3.2 level. The succession of the phenomena suggests that the flare processes were induced by eruption E2. Observations do not support a suggestion of Kumar, Manoharan, and Uddin (2011) that ‘the energy release at the first stage of the M3.2 flare (*i.e.*, E1) triggered the first ejection (E2)’. As Figure 2d shows, the major energy release of event E1 that was observed in HXR and microwave bursts ceased well before the onset of eruption E2. As mentioned, this eruption was probably triggered by photospheric motions.

Eruption E2 disturbed filament F1, which probably was in a metastable state. Its apparent twitch in the $\text{H}\alpha$ images that started just after E2 suggests perturbations of plasma flows in the filament. The filament was initially inclined by $\sim 23^\circ$ to the line of sight and started to lift off following the neutral surface. It moved up and South-West and underwent, at least, two acceleration phases. The first acceleration pulse peaked at 07:44:30 ($\approx 110 \text{ m s}^{-2}$), slightly later than the acceleration of E2, up to a speed of about 35 km s^{-1} . The second acceleration pulse peaked at about 07:57 (episode E3; $\approx 170 \text{ m s}^{-2}$) and resulted in a final speed of $\approx 110 \text{ km s}^{-1}$. These plane-of-sky velocities agree with the line-of-sight ones implied by the $\text{H}\alpha$ wings. The latest observation of filament fragments in the far-blue $\text{H}\alpha$ wing ($\lambda = 6562.8 - 1.770 \text{ \AA}$) at 08:15:20 (Figures 1b and 6d) suggesting upwards velocities of $64 - 96 \text{ km s}^{-1}$ also agrees with the overall kinematics. A weak microwave response to the significant acceleration during episode E3 was certainly present (Figure 2d). The close temporal correspondence between the acceleration episodes of the filament and the flare bursts provides further support for the active roles of the filament itself and plasma flows in the filament.

The temporal correspondence between the acceleration of a CME and flare emissions has been found by Zhang *et al.* (2001) and Temmer *et al.* (2008; 2010). Reconnection in a sheared arcade significantly increases the poloidal magnetic field in the developing flux rope that was quantitatively confirmed by Qiu *et al.* (2007). Due to the curvature of the flux rope, the toroidal force propelling its expansion increases. After impulsive acceleration, the poloidal ‘mainspring’ relaxes and the toroidal force ceases, while the flux rope continues to expand with an increased speed. This booster mechanism (see, *e.g.*, Vršnak, 2008) seems to be commonly present in flare-related eruptions. This probably occurred in the faint episode E3, when the filament impulsively accelerated.

The accelerated filament laminated. Its parts showed rather wide acceleration temporal ranges, maximum accelerations, and speeds. The strongest acceleration of $\gtrsim 500 \text{ m s}^{-2}$ and highest speed ($\approx 210 \text{ km s}^{-1}$) were measured along the North horn of the Y-darkening, where acceleration peaked after 08:02.

The direction of the filament’s motion crossed an unavoidable topological obstacle. As mentioned, a rising eruptive filament is known to successively reproduce in its motion the contours of the same neutral line of Br changing with height. The topology of the neutral lines broke in the saddle region of the neutral surface (Figure 17), and the filament had no chance to retain its former configuration and integrity after passing through this region. Having encountered this obstacle above region Rb at about 08:07 (episode E4A), the filament apparently bifurcated into two components F1’ and F1’’. Both upwards and downwards motions of these components are indicated by the red and blue $H\alpha$ wings. The collision probably resulted in reconnection between magnetic structures of the filament with environment magnetic fields.

This assumption is supported by the correspondence between the $H\alpha$ and SXR flare-like response in the bifurcation region and the HXR peaks E4A and E4B in active region 501 in the interval from 08:07 to 08:13 because the pre-eruptive filament does not seem to be connected to this region. After that the bifurcated filament apparently transformed into two wide diverging jets constituting the Y-like cloud carrying predominantly cool filament material to remote sites on the solar surface. The SPIRIT images show them at 304 \AA up to the South-West of the limb (08:23–09:55). The cloud consisted of dispersed fragments of the filament with wide ranges of speeds and directions of motion within a sector of about 60° in the plane of the sky and some vertical scatter. The transformation of the filament into the Y-like cloud is confirmed by the correspondence between their masses, as well as their common kinematics. Neither off-limb extensions of the Y-like cloud, nor a corresponding slow CME are detectable. Plasma flows from this cloud away from the Sun are not excluded, while probably most of the mass eventually fell back on the solar surface far from the eruption site.

In the outlined scenario, reconnection increases the poloidal flux of an ascending flux rope and completes its formation pushing the rope into the interplanetary space. In the 18 November event, a portion of the poloidal flux possibly escaped with the Y-like cloud coming from the filament. Most of its mass was not ejected into the interplanetary space. The poloidal flux of this structure could partly be lost in magnetic reconnection with coronal magnetic fields and partly carried away as an almost empty structure invisible in white light. This

circumstance might account for the significant excess of the reconnected magnetic flux with respect to the MC found by Möstl *et al.* (2008) and attributed by the authors to reconnection between the MC and interplanetary magnetic fields. Moreover, the unusual scenario of the filament eruption revealed by our analysis makes relating the flare reconnection flux with the 20 November MC questionable.

The probable scenario of sequential eruptions and subsequent transformation of the filament in the 18 November 2003 event looks unusual, but this event was not exceptional in this respect. A similar anomalous eruption was discussed by Grechnev *et al.* (2008). The transit of an eruptive filament through a coronal magnetic null point (see, *e.g.*, Gary and Moore, 2004) can transform the filament into an eruptive jet (Meshalkina *et al.*, 2009; Filippov, Golub, and Koutchmy, 2009). Grechnev *et al.* (2011a) presented other candidates for anomalous eruptions and showed their probable correlation with the so-called negative radio bursts (decreases of the total microwave flux below a quasi-stationary level) without a one-to-one correspondence. A negative burst could not be observed in the 18 November event, because the anomalous eruption was followed by ongoing flaring. The authors suggested anomalous eruptions to be favored by complex magnetic configurations and surrounding of the active region by others, and did not expect an anomalous eruption of a quiescent filament beyond an activity complex. The clearest example of anomalous eruption was observed by SDO/AIA on 7 June 2011 between 06:15 and 10:00 when dispersed absorbing fragments of a disintegrating filament were well visible even in the 193 Å images without subtraction. The “destruction” of the magnetic structure of an eruptive filament in such anomalous eruptions deserves the attention of future studies.

The anomalous character of the main eruption in the 18 November 2003 event brings the attention to CME2 (Figure 1c). Its faint, fast outer halo envelope crossing a distorted streamer could be a trace of a shock wave (Grechnev *et al.*, 2011b, section 4.3.2) excited by one of sharp eruptions. The initiation time of the inner component estimated by Gopalswamy *et al.* (2005c) suggests its development in the complex E4 event. The appearance of the inner component corresponds to the pointing of the pre-eruptive filament F1 and its initial non-radial motion. Remarkable is a radial structure of the inner component suggesting its development from an arcade which was initially located above the filament or its trajectory, and then expanded being forced to erupt. Neither cavity nor core were clearly evident, whereas a threadlike core (former filament) is typically a brightest CME component. These features of CME2 are consistent with our conclusion that the bulk of the filament material had not left the Sun (*cf.* Grechnev *et al.*, 2008; 2011a). We will consider CME2 in more detail in paper II.

A possible extra eruption seems to have occurred between 08:07 and 08:17 close to the disk center. This eruption is suggested by the central dimming in the images of GOES/SXI (Figure 8i), SPIRIT 175 Å (Figure 9b–c), and EIT (Figure 1c) as well as the ‘disconnection’ of the bifurcation region from the flare site shown by the H α and HXR time profiles between events E4B and E4C in Figure 8g. Similar manifestations of disconnection were considered by Kundu *et al.* (2001) and Grechnev, White, and Kundu (2003) as indications of changes in

the magnetic connectivity during solar flares. The presumable eruption between 08:07 and 08:17 could result in one extra CME, which might not be detected in LASCO images. This issue will be addressed in papers II and III.

We have found out what happened to the main filament mass, but it is not so clear what happened to its magnetic flux. Part of it might be carried away frozen in the Y-like inheritor of the bifurcated filament. Some part of the magnetic flux probably reconnected during the interaction with the bifurcation region. The final outcome is uncertain. Anyway, these circumstances make doubtful a simple scenario, in which the magnetic cloud hitting Earth is considered as a stretched flux rope formed from a structure initially associated with the pre-eruption filament F1. Grechnev *et al.* (2005) concluded that in the 18 November event ‘the eruptive filament probably failed to become the CME core’, but this result was not considered by other authors who analyzed the causes of the extreme geoeffective disturbance and its possible solar source. They will be revisited in paper IV.

The challenges revealed in preceding studies of the 20 November magnetic cloud and its presumable solar source, extended by our results, are as follows:

1. Very strong magnetic field in the MC that was close to a record value.
2. Different handedness of the MC and the presumed solar source.
3. Different orientations of the magnetic field in the MC and the presumed solar source ($> 90^\circ$, Möstl *et al.*, 2008).
4. Implication of CME1 looks doubtful, because a similar CME in the stronger 17 November event was not geoeffective.
5. Responsibility of the moderately fast coreless CME2 for the severest geomagnetic storm seems to be unlikely.

Items (2) and (3) indicate that the commonly assumed association of the MC with the U-shaped filament in AR 501 is questionable. The suggestions of the eruption which presumably occurred between 08:07 and 08:17 imply the development of an extra CME. If this hypothetical CME expanded exactly earthward from the solar disk center within a very narrow cone, then the Thomson-scattered light was meager to be detected by LASCO. Such atypically weak expansion of the CME must result in very strong magnetic field inside due to magnetic flux conservation. Paper II addresses further suggestions of this possible CME.

7. Conclusion

To complement the picture of the complex 18 November 2003 event established in preceding papers, we have studied a succession of eruptions and the corresponding flare episodes E1, E2, E3, and E4 in the interval 07:29 to 08:30. We have measured the kinematic properties of eruptive filaments and found that they underwent impulsive acceleration episodes, which were temporally close to microwave/HXR bursts. The eruptions rapidly expanded and lost opacity which made difficult their subsequent observation. Nevertheless, it was possible to reveal their further evolution. Our results and their implications are as follows.

1. *Triggers and mechanisms of eruptions.* Probable primary triggers of the partial eruptions at 07:29 (E1) and 07:41 (E2) were photospheric motions. Eruption E2 presumably occurred due to rapid heating of a long filament segment probably caused by an MHD disturbance. The corresponding sharp pressure increase in the filament could induce an ejection of some part of its material along the magnetic field. In turn, the disturbance produced by eruption E2 most likely destabilized filament F1 and triggered its eruption at 07:56 (E3).
2. *Filament eruptions and CME initiation.* The eruptions presumably initiated the CMEs. Development of the eruptions after their triggers by the factors listed above appears to be self-sufficient so that outer drivers do not seem to be required. This circumstance is important for models of eruptions and initiation of CMEs, while eruptive filaments are often considered to be passive structures being pulled upwards by larger-scale magnetic ropes.
3. *Anomalous eruption.* The major eruption was anomalous; after the initial lift-off, the eruptive filament bifurcated and had not left the Sun as a whole, while its main mass probably fell back on the solar surface. This anomaly occurred due to the collision around 08:07 of the eruptive filament with an unavoidable topological discontinuity—a magnetic null point. Being not able to pass through the obstacle keeping integrity, the filament bifurcated. Flare episodes E4A (08:09) and E4B (08:12) responded to this process.
4. *The problem of the geomagnetic impact.* Relation to the 20 November 2003 magnetic cloud is doubtful for the 07:29 eruption presumedly associated with CME1 and the 07:41 eruption, which most likely had not produced any CME at all. The transformation of the eruptive filament, whose main part had not left the Sun, contradicts simple considerations of the magnetic cloud hitting the Earth as a stretched magnetic flux-rope formed from a structure initially associated with the pre-eruption filament. On the other hand, a possible additional eruption, which appears to have occurred between 08:07 and 08:17 close to the solar disk center, might be implicated in the development of a structure responsible for the geomagnetic superstorm. Further substantiation of this scenario will be presented in Papers II to IV.

Acknowledgements We thank Viktoria Kurt for the CORONAS-F/SONG data, L. Kashapova and S. Kalashnikov for the assistance in data processing, and I. Kuzmenko for useful discussions. We are grateful to an anonymous reviewer for valuable recommendations to improve the paper. We thank the instrumental teams of the Kanzelhöhe Solar Observatory; TRACE and CORONAS-F missions; MDI, EIT, and LASCO on SOHO (ESA & NASA); the USAF RSTN Radio Solar Telescope Network; and the GOES satellites for the data used here.

This study was supported by the Russian Foundation of Basic Research under grants 11-02-00757, 11-02-01079, 12-02-00008, 12-02-92692, and 12-02-00037, the Program of basic research of the RAS Presidium No. 22, and the Russian Ministry of Education and Science under State Contract 16.518.11.7065. The research was also partly supported by the European Commission’s Seventh Framework Programme (FP7/2007-2013) under the grant agreement eHeroes (project No. 284461), www.eheroes.eu.

References

- Anzer, U., Heinzel, P.: 2005, *Astrophys. J.* **622**, 714.
 Aulanier, G. Schmieder, B.: 2002, *Astron. Astrophys.* **386**, 1106.

- Bogachev, S.A., Grechnev, V.V., Kuzin, S.V., Slemzin, V.A., Bugaenko, O.I., Chertok, I.M.: 2009, *Solar Sys. Res.* **43**, 143.
- Brueckner, G.E., Howard, R.A., Koomen, M.J., Korendyke, C.M., Michels, D.J., Moses, J.D., Socker, D.G., Dere, K.P., *et al.*: 1995, *Solar Phys.* **162**, 357.
- Carrington, R.C.: 1859, *Mon. Not. Roy. Astron. Soc.* **20**, 13.
- Chandra R., Pariat, E., Schmieder, B., Mandrini, C.H., Uddin, W.: 2010, *Solar Phys.* **261**, 127.
- Chertok, I.M., Grechnev, V.V.: 2005, *Astron. Rep.* **49**, 155.
- d'Azambuja, M., d'Azambuja, L.: 1948, *Ann. Obs. Paris, Meudon* **6**, Fasc. VII.
- Delaboudinière, J.-P., Artzner, G.E., Brunaud, J., Gabriel, A.H., Hochedez, J.-F., Millier, F., Song, X.Y., Au, B., *et al.*: 1995, *Solar Phys.* **162**, 291.
- Démoulin, P., Aulanier, G.: 2010, *Astrophys. J.* **718**, 1388.
- Echer, E., Gonzalez, W.D., and Tsurutani, B.T.: 2008, *Geophys. Res. Lett.* **350**, 6.
- Filippov, B.P., Den, O.G.: 2001, *J. Geophys. Res.* **106**, 25177.
- Filippov, B., Golub, L., Koutchmy, S.: 2009, *Solar Phys.* **254**, 259.
- Filippov, B.P., Gopalswamy, N., Lozhechkin, A.V.: 2001, *Solar Phys.* **203**, 119.
- Filippov, B.P., Gopalswamy, N., Lozhechkin, A.V.: 2002, *Astron. Rep.* **46**, 417.
- Filippov, B., Koutchmy, S.: 2008, *Ann. Geophys.* **26**, 3025.
- Gary, G. A., Moore, R. L.: 2004, *Astrophys. J.* **611**, 545.
- Gopalswamy, N., Barbieri, L., Cliver, E.W., Lu, G., Plunkett, S.P., Skoug, R.M.: 2005a, *J. Geophys. Res.* **110**, A09S00.
- Gopalswamy, N., Yashiro, S., Liu, Y., Michalek, G., Vourlidis, A., Kaiser, M.L., Howard, R.A.: 2005b, *J. Geophys. Res.* **110**, A09S15.
- Gopalswamy, N., Yashiro, S., Michalek, G., Xie, H., Lepping, R.P., Howard, R.A.: 2005c, *Geophys. Res. Lett.* **32**, L12S09.
- Grechnev, V.V.: 2003, *Solar Phys.* **213**, 103.
- Grechnev, V.V., White, S.M., Kundu, M.R.: 2003, *Astrophys. J.* **588**, 1163.
- Grechnev, V.V., Chertok, I.M., Slemzin, V.A., Kuzin, S.V., Ignat'ev, A.P., Pertsov, A.A., Zhitnik, I.A., Delaboudinière, J.-P., Auchère, F.: 2005, *J. Geophys. Res.* **110**, A09S07.
- Grechnev, V.V., Uralov, A.M., Zandanov, V.G., Baranov, N.Y., Shibasaki, K.: 2006, *Pub. Astron. Soc. Japan* **58**, 69.
- Grechnev, V.V., Uralov, A.M., Slemzin, V.A., Chertok, I.M., Kuzmenko, I.V., Shibasaki, K.: 2008, *Solar Phys.* **253**, 263.
- Grechnev, V.V., Kuzmenko, I.V., Chertok, I.M., Uralov, A.M.: 2011a, *Astron. Rep.* **55**, 637.
- Grechnev, V.V., Uralov, A.M., Chertok, I.M., Kuzmenko, I.V., Afanasyev, A.N., Meshalkina, N.S., Kalashnikov, S.S., Kubo, Y.: 2011b, *Solar Phys.* **273**, 433.
- Handy, B.N., Acton, L.W., Kankelborg, C.C., Wolfson, C.J., Akin, D.J., Bruner, M.E., Carvalho, R., Catura, R.C., *et al.*: 1999, *Solar Phys.* **187**, 229.
- Heinzel, P., Anzer, U., Schmieder, B.: 2003a, *Solar Phys.* **216**, 159.
- Heinzel, P., Anzer, U., Schmieder, B., Schwartz, P.: 2003b, *ESA SP-535*, 447.
- Hill, S.M., Pizzo, V.J., Balch, C.C., Biesecker, D.A., Bornmann, P., Hildner, E., *et al.*: 2005, *Solar Phys.* **226**, 255.
- Ivanov, K.G., Romashets, E.P., Kharshiladze, A.F.: 2006, *Geomag. and Aeron.* **46**, 275.
- Kumar, P., Manoharan, P.K., Uddin, W.: 2011, *Solar Phys.* **271**, 149.
- Kundu, M.R., Grechnev, V.V., Garaimov, V.I., White, S.M.: 2001, *Astrophys. J.* **563**, 389.
- Kuznetsov, S.N., Kurt, V.G., Yushkov, B.Y., Kudela, K., Galkin, V.I.: 2011, *Solar Phys.* **268**, 175.
- Lin, R.P., Dennis, B.R., Hurford, G.J., Smith, D.M., Zehnder, A., Harvey, P.R., *et al.*: 2002, *Solar Phys.* **210**, 3.
- Lui, A.T.Y.: 2011, *Space Sci. Rev.* **158**, 43.
- Mackay, D.H., Karpen, J.T., Ballester, J.L., Schmieder, B., Aulanier, G.: 2010, *Space Sci. Rev.* **151**, 333.
- Maričić, D., Vršnak, B., Stanger, A.L., Veronig, A.: 2004, *Solar Phys.* **225**, 337.
- Maričić, D., Vršnak, B., Stanger, A.L., Veronig, A.M., Temmer, M., Roša, D.: 2007, *Solar Phys.* **241**, 99.
- Mein, N., Mein, P., Heinzel, P., Vial, J.-C., Malherbe, J.M., Staiger, J.: 1996, *Astron. Astrophys.* **309**, 275.
- Meshalkina, N. S., Uralov, A. M., Grechnev, V. V., Altyntsev, A. T., Kashapova, L. K.: 2009, *Pub. Astron. Soc. Japan* **61**, 791.
- Miklenic, C.H., Veronig, A.M., Vršnak, B., Hanslmeier, A.: 2007, *Astron. Astrophys.* **461**, 697.

- Miklenic, C.H., Veronig, A.M., Vršnak, B.: 2009, *Astron. Astrophys.* **499**, 893.
- Molodensky, M.M., Filippov, B.P.: 1987, *Sov. Astronom.* **31**, 564.
- Möstl, C., Miklenic, C., Farrugia, C.J., Temmer, M., Veronig, A., Galvin, A.B., Vršnak, B., Biernat, H.K.: 2008, *Ann. Geophys.* **26**, 3139.
- Molowny-Horas, R., Heinzel, P., Mein, P., Mein, N.: 1999, *Astron. Astrophys.* **345**, 618.
- Neupert, W. M.: 1968, *Astrophys. J.* **153**, L59.
- Oraevsky, V.N., Sobelman, I.I.: 2002, *Astron. Lett.* **28**, 401.
- Oraevsky, V.N., Sobelman, I.I., Zitnik, I.A., Kuznetsov, V.D., Stepanov, A.I., Polishuk, G.M., et al.: 2003, *Adv. Spa. Res.* **32**, 2567.
- Pizzo, V.J., Hill, S.M., Balch, C.C., Biesecker, D.A., Bornmann, P., Hildner, E., et al.: 2005, *Solar Phys.* **226**, 283.
- Qiu, J., Hu, Q., Howard, T.A., Yurchyshyn, V.B.: 2007, *Astrophys. J.* **659**, 758.
- Rompolt, B.: 1998, *IAU Colloq. 167: New Perspectives on Solar Prominences* **150**, 330.
- Rudenko, G.V.: 2001, *Solar Phys.* **198**, 5.
- Rudenko, G. V., Grechnev, V. V.: 1999, *Astronomical Data Analysis Software and Systems VIII*, ASP Conf. Series, **172**, 421.
- Scherrer, P. H., Bogart, R. S., Bush, R. I., Hoeksema, J. T., Kosovichev, A. G., Schou, J., et al.: 1995, *Solar Phys.* **162**, 129.
- Slemzin, V., Chertok, I., Grechnev, V., Ignat'ev A., Kuzin S., Pertsov A., Zhitnik I., Delaboudinière J.-P.: 2004, In A.V. Stepanov, E.E. Benevolenskaya, and A.G. Kosovichev, editors, *Multi-Wavelength Investigations of Solar Activity*, *Proc. IAU Symp. 223*, 533.
- Slemzin, V.A., Kuzin, S.V., Zhitnik, I.A., Delaboudinière, J.-P., Auchere, F., Zhukov, A.N., van der Linden, R., Bugaenko, O.I., Ignat'ev, A.P., Mitrofanov, A.V., Pertsov, A.A., Oparin, S.N., Stepanov, A.I., Afanas'ev, A.N.: 2005, *Solar Sys. Res.* **39**, 489.
- Srivastava, N., Mathew, S.K., Louis, R.E., Wiegelmann, T.: 2009, *J. Geophys. Res.* **114**, A03107.
- Temmer, M., Veronig, A.M., Vršnak, B., Rybák, J., Gömöry, J., Stoiser, S., Maričić, D.: 2008, *Astrophys. J.* **673**, L95.
- Temmer, M., Veronig, A.M., Kontar, E.P., Krucker, S., Vršnak, B.: 2010, *Astrophys. J.* **712**, 1410.
- van Tend, W., Kuperus, M.: 1978, *Solar Phys.* **59**, 115.
- Tsurutani, B.T., Gonzalez, W.D., Lakhina, G.S., Alex, S.: 2003, *J. Geophys. Res. A* **108**, 1268.
- Veselovsky, I.S., Panasyuk, M.I., Avdyushin, S.I., Bazilevskaya, G.A., Belov, A.V., Bogachev, S.A. et al.: 2004, *Cosmic Res.* **42**, 435.
- Vršnak, B.: 2008, *Ann. Geophys.* **26**, 3089.
- Wang, Y., Zhang, J., Shen, C.: 2009, *J. Geophys. Res.* **114**, 10104.
- Yashiro, S., Gopalswamy, N., Michalek, G., St. Cyr, O. C., Plunkett, S. P., Rich, N. B., Howard, R. A.: 2004, *J. Geophys. Res.* 109, A07105.
- Yermolaev Yu.I., Zelenyi, L.M., Zastenker, G.N., et al.: 2005, *Geomag. and Aeron.*, **45**, 20.
- Yurchyshyn, V., Hu, Q., Abramenko, V.: 2005, *Space Weather*, **3**, S08C02.
- Zagnetko, A.M., Filippov, B.P., Den, O.G.: 2005, *Astron. Rep.* **49**, 425.
- Zhang, J., Dere, K.P., Howard, R.A., Kundu, M.R., White, S.M.: 2001, *Astrophys. J.* **559**, 452.
- Zhitnik, I.A., Bougaenko, O.I., Delaboudinière, J.-P., Ignatiev, A.P., Korneev, V.V., Krutov, V.V., Kuzin, S.V., Lisin, D.V., et al.: 2002, *Proc. 10th European Solar Physics Meeting, Prague (ESA SP-506)*, 915.